

Toward a multivariate formulation of the PKF assimilation: application to a simplified chemical transport model

Antoine Perrot¹, Olivier Pannekoucke^{1,2,3}, and Vincent Guidard¹

¹CNRM, Université de Toulouse, Météo-France, CNRS, Toulouse, France

²CERFACS, Toulouse, France

³INPT-ENM, Toulouse, France

Correspondence: Olivier Pannekoucke (olivier.pannekoucke@meteo.fr)

Abstract. This contribution explores a new approach to forecast multivariate covariances for atmospheric chemistry through the use of the parametric Kalman filter (PKF). In the PKF formalism, the error covariance matrix is modeled by a covariance model relying on parameters, for which the dynamics is then computed. The PKF has been previously formulated in univariate cases, and a multivariate extension for chemical transport models is explored here. This contribution focuses on the situation where the uncertainty is due to the chemistry but not due to the uncertainty of the weather. To do so, a simplified two-species chemical transport model over a 1D domain is introduced, based on the nonlinear Lotka-Volterra equations, which allows to propose a multivariate pseudo covariance model. Then, the multivariate PKF dynamics is formulated and its results are compared with a large ensemble Kalman filter (EnKF) in several numerical experiments. In these experiments, the PKF accurately reproduces the EnKF. Eventually, the PKF is formulated for a more complex chemical model composed of six chemical species (Generic Reaction Set). Again, the PKF succeeds at reproducing the multivariate covariances diagnosed on the large ensemble.

1 Introduction

Data assimilation aims to provide an estimation of the true state of a system. This estimation, called the analysis, is a compromise between the forecast of the state and the available observations. The optimal combination of the forecast and the observations relies on their respective error covariance matrices as given by the Kalman filter equations (Kalman, 1960). The accuracy of the analysis is directly related to the quality of these two matrices.

In atmospheric chemistry applications, the system to study is the concentration of multiple chemical species in the atmosphere. In most cases, chemical transport models (CTMs) are used to forecast the concentrations, as the operational model MOCAGE used in Météo-France (Josse et al., 2004). CTMs make predictions based on the transport by the wind (the fields are provided by NWP models) and the chemical interactions of the species (Hauglustaine et al., 1998) ; and takes into account multiple other important processes *e.g.* the diffusion, the emissions, the deposition or the interaction with clouds. However, in CTMs chemistry do not influence the meteorology, which is of course a crude approximation of the true atmosphere. The advantage of a CTMs is that it allows air quality prediction at a low numerical cost, and is used in several operational centers. For

instance, the CAMS regional air quality production ¹, which daily forecast a multi-model ensemble of 11 members that covers
25 the following 4 days, is performed from the integration of 11 models from which 10 are CTMs. Note that each member of the
ensemble relies on its own data assimilation system for providing its surface analysis, while all models process the same set
of surface observations, and all model forecasts are based on the same meteorological forcings from ECMWF high resolution
weather forecasts. In particular, members of the CAMS multi-model ensemble are not used within an EnKF to provide its own
assimilation system.

30 In this context, the forecast-error covariance matrix contains the correlations of the forecast errors within and between the
chemical species. In multivariate covariance modeling applied in meteorology, these correlations are respectively denoted by
autocorrelations and *cross-correlations* (Derber and Bouttier, 1999). Accurately describing the auto and cross-correlation is a
key component for improving the overall quality of the analysis. Indeed, strong correlations exist between different chemical
species, and the analysis could benefit from them: an observation for a given species might also correct other concentrations
35 and reduce their error amplitude at the same time. Note that in operational applications, chemical species are often assimilated
separately *e.g.* in CAMS 2.40, the univariate 3DVar system of MOCAGE is used for the assimilation of ozone, nitrogen
dioxide, sulphur dioxide, and fine particulate matter PM2.5 and PM10 (following a configuration similar to the one used for
MACII detailed by Marécal et al. (2015)). Note also that simplifications are often introduced to represent a flow dependency of
the background term *e.g.* in several studies using MOCAGE, the 3DVar background error standard deviations are specified as a
40 percentage of the first guess field (Amraoui et al., 2020; Aabaribaoune et al., 2021; Peiro et al., 2018) – which is very different
from the forecast error variance in an EnKF that results from the ensemble estimation and the dynamics of the uncertainty
along the previous analysis and forecast cycles.

However, the estimation and the modelling of multivariate covariances in air quality is a complex topic (Emili et al., 2016).
But this is not specific to air quality, and two main approaches are found in data assimilation. The first one relies on balance
45 operators and has been introduced in variational data assimilation. These balance operators establish a relation between the
state variables and allow for the modelling of cross-covariances from the design of univariate covariances. Such operators
exist in numerical weather prediction (Derber and Bouttier, 1999; Fisher, 2003) as well as for the ocean (Weaver et al., 2006),
but as far as we know, no balance operators are used in atmospheric chemistry applications. The second approach relies on
the ensemble method (Evensen, 2009) where an ensemble of forecasts is used to estimate the multivariate covariance matrix
50 (Coman et al., 2012). The ensemble method offers a flow dependent estimation of the error statistics and leads to a practical
implementation of the Kalman filter, that is the ensemble Kalman filter (EnKF) (Evensen, 1994). The EnKF applies to a wide
range of problems, from a simple Lorenz 63 model (Lorenz, 1963) to the numerical prediction of the atmosphere or the ocean.
At the same time, this advantage may be seen as a limitation: the EnKF not necessarily takes advantage of the particular
set of equations of a problem *e.g.* the continuity of physical fields which leads to simplification not available in the usual
55 matrix formulation of the EnKF equations. Moreover the ensemble method presents some drawbacks. For instance, since the

¹<https://atmosphere.copernicus.eu/cams-european-air-quality-ensemble-forecasts-welcomes-two-new-state-art-models>, associated with CAMS2.40
<https://confluence.ecmwf.int/display/CKB/CAMS+Regional%3A+European+air+quality+analysis+and+forecast+data+documentation> see here for scientific
description – last access to web references: 15 March 2023)

estimation often relies on a small ensemble, the statistical estimations are polluted by a spurious sampling noise which requires the introduction of filtering (Berre et al., 2007) and localization (Houtekamer and Mitchell, 1998, 2001). In air quality, it may be preferable to set the ensemble estimation of the multivariate correlation to zero, to avoid polluting the resulting analysis state (Tang et al., 2011; Gaubert et al., 2014), except at the globe surface (Eben et al., 2005) or when the chemical species are strongly correlated (Miyazaki et al., 2012). Note that additional treatments can be required as inflation of the variance in order to represent effects of model errors (Anderson and Anderson, 1999; Whitaker and Hamill, 2003). As another drawback, the numerical computation of the EnKF is costly since it relies on the several time integrations of a numerical model, which are often computed in parallel at lower resolution.

Recently, a new approximation of the KF has been introduced, the parametric Kalman filter (PKF), where the error covariance matrices are approximated by a covariance model fitted with a set of parameters *e.g.* the grid-point variance and the local anisotropy (Pannekoucke et al., 2016). In the PKF, the dynamics of the parameters are described all along the forecast and analysis steps of the assimilation cycle (Pannekoucke, 2021). This approach does not rely on ensembles, and the dynamics of the parameters is deduced from the partial differential equations that govern the physical system. Hence, the PKF opens the way to understanding the physics of uncertainties. However, the construction of the parameter dynamics is the most difficult part for the design of the PKF. When the parameters are the variance and the local error-correlation anisotropy, a systematic formalism for deducing PKF's equations based on a Reynolds decomposition (or Reynolds averaging technique see *e.g.* Lesieur, chap. 4) has been introduced associated with a Python package, SymPKF (Pannekoucke and Arbogast, 2021), and is based on the Python computer algebra system SymPy (Meurer et al., 2017). But, modeling the physics of uncertainties often comes with closure problems. To alleviate this issue, another numerical framework, PDE-Netgen has been introduced to be able to close problems using a deep learning approach (Pannekoucke and Fablet, 2020).

Applying the PKF approach for CTMs is attractive because the parametric dynamics is known for the transport equations (Cohn, 1993; Pannekoucke et al., 2018), and this leads to a better understanding of the forecast-error covariance dynamics *e.g.* a better understanding of the model-error covariance due to the numerical integration (Pannekoucke et al., 2021), and the loss of variance which appears in the EnKF (Ménard et al., 2021). Moreover, an application of the PKF has been recently proposed for the assimilation of GOSAT methane in the hemispheric CMAQ model (Voshtani et al., 2022a, b), showing the potential of the PKF in nearly operational applications where only the error variance evolved. Compared to specifying the background variance as a percentage of the first guess, as mentioned above for the MOCAGE assimilation, the PKF could provide a flow dependence more consistent with the KF theoretical framework, but without the numerical cost of using an ensemble as with an EnKF.

While the PKF has been formulated for univariate statistics, a first attempt in multivariate statistics has been proposed, based on the balance operator approach (Pannekoucke, 2021). However, applying such a balance operator is a challenge for chemical reactions where no simple relation exists as the geostrophic balance in weather forecasting. Hence, the aim of this contribution is to explore how to extend the univariate PKF into a multivariate formulation adapted to CTMs. To do so, a multivariate covariance model adapted to air quality prediction is first proposed and then it is validated by a twin experiment based on an EnKF using a large ensemble.

This contributions only focuses on the uncertainty dynamics due to the chemistry without accounting for the part of the uncertainty of the weather *e.g.* we do not take into account the uncertainty of the wind that transports the chemical species.

The paper is organized as follows. Section 2 reminds basic concepts in data assimilation with the formalism of the Kalman Filter and its parametric approximation in univariate statistics. Then, in Section 3, a simplified two species multivariate CTM is introduced for which a multivariate parametric assimilation is first proposed then validated based on a comparison with an ensemble approach. A six-species chemical scheme is considered in Section 4 to evaluate the PKF multivariate forecast in a more complex context. The conclusions of the contribution are given in Section 5

2 Background on the Parametric Kalman Filter

The parametric Kalman filter (PKF) is a recent implementation of the Kalman filter where the covariance matrices are approximated by some covariance model. For the sake of consistency, this section first recaps the basics of the Kalman filter, then it reminds the diagnosis of covariance matrix in large dimension and covariance models to introduce the formalism of the PKF in univariate statistics. The section ends with a numerical example of interest for air quality that illustrates the PKF

2.1 Analysis and forecast step in the Kalman filter

Here we consider a system whose state is denoted by \mathcal{X} and governed by the evolution equation

$$\partial_t \mathcal{X} = \mathcal{M}(\mathcal{X}). \quad (1)$$

Time integration from a time t_q to a time t_{q+1} of the dynamics Eq. (1) defines the propagator $\mathcal{M}_{t_{q+1} \leftarrow t_q}$, that maps a state $\mathcal{X}(t_q)$ to the prediction of Eq. (1), $\mathcal{X}(t_{q+1}) = \mathcal{M}_{t_{q+1} \leftarrow t_q} \mathcal{X}(t_q)$. In geophysics, \mathcal{X} stands for the multivariate fields that represent the state of the ocean, the atmosphere or chemical species concentration for air quality. The dynamics \mathcal{M} is then given by a system of partial differential equations. After spatial discretization, \mathcal{M} becomes a system of ordinary differential equations, and \mathcal{X} is a vector of dimension n . Thereafter, \mathcal{X} can be seen either as a collection of continuous fields with dynamics given by Eq. (1) or a discrete vector of dynamics the discretized version of Eq. (1).

Because of the spatio-temporal sparsity of observations, as well as modeling, chaotically amplification of initial error in forecast and measurement errors, the exact actual state at a time $t = t_q$, \mathcal{X}_q^t , is unknown.

Data assimilation aims to provide the analysis state, \mathcal{X}_q^a , that is an estimation of \mathcal{X}_q^t performed from the observations and the forecast state. The analysis state is decomposed into $\mathcal{X}_q^a = \mathcal{X}_q^t + \varepsilon_q^a$ where ε_q^a is the analysis error, which is modeled as a random error of zero mean and covariance matrix $\mathbf{P}_q^a = \mathbb{E}(\varepsilon_q^a (\varepsilon_q^a)^T)$, with \mathbb{E} (or its shorthand $\bar{\cdot}$) the expectation operator, and T the transpose operator. This analysis state \mathcal{X}_q^a can be obtained by combining the forecast state \mathcal{X}_q^f and the observations \mathcal{Y}_q^{obs} . Similarly, to the analysis state, the forecast and the observations can be written as $\mathcal{X}_q^f = \mathcal{X}_q^t + \varepsilon_q^f$ and $\mathcal{Y}_q^{obs} = Y_q^t + \varepsilon_q^{obs}$ introducing the forecast (the observation) error ε_q^f (ε_q^{obs}), both modelled as random errors of zero mean and covariance matrices $\mathbf{P}_q^f = \mathbb{E}(\varepsilon_q^f (\varepsilon_q^f)^T)$ and $\mathbf{R}_q = \mathbb{E}(\varepsilon_q^{obs} (\varepsilon_q^{obs})^T)$ respectively. In the case where the dynamic of \mathcal{X}^t is assumed linear, replacing \mathcal{M} by its matrix version \mathbf{M} in Eq. (1); and when the errors are Gaussian, uncorrelated in time, and errors between observations

and forecast are independent, the Kalman filter's equations (KF) describe the evolution of the uncertainty over time (Kalman, 1960).

The process of estimating the analysis state from a forecast and some observations is called the analysis step. The forecast error covariance matrix denoted by \mathbf{P}_q^f and the observation error covariance matrix \mathbf{R}_q associated respectively with \mathcal{X}_q^f and \mathcal{Y}_q^{obs} , are used to produce the optimal estimation (*analysis*) \mathcal{X}_q^a of \mathcal{X}_q^t , and the associated analysis-error covariance matrix \mathbf{P}_q^a . The equations of this procedure are:

$$\mathcal{X}_q^a = \mathcal{X}_q^f + \mathbf{K}_q (\mathcal{Y}_q^{obs} - \mathbf{H}_q \mathcal{X}_q^f), \quad (2a)$$

$$\mathbf{P}_q^a = (\mathbf{I}_n - \mathbf{K}_q \mathbf{H}_q) \mathbf{P}_q^f, \quad (2b)$$

130 where $\mathbf{K}_q = \mathbf{P}_q^f \mathbf{H}_q^T (\mathbf{H}_q \mathbf{P}_q^f \mathbf{H}_q^T + \mathbf{R}_q)^{-1}$ is the Kalman gain matrix with \mathbf{H}_q the linear observation operator that maps the state vector into the observation space; \mathbf{P}_q^a is the analysis error covariance matrix ; and \mathbf{I}_n the identity matrix in dimension n .

Next, the forecast step pushes the uncertainty forward in time. The analysis state \mathcal{X}_q^a is propagated using the linear dynamics \mathbf{M} to obtain the forecast \mathcal{X}_{q+1}^f at time t_{q+1} leading to an estimation of the true state system $\mathcal{X}^t(t_{q+1})$. The Gaussian error statistics for this forecast are given by the Kalman filter forecast step

$$135 \mathcal{X}_{q+1}^f = \mathbf{M}_{q+1 \leftarrow q} \mathcal{X}_q^a, \quad (3a)$$

$$\mathbf{P}_{q+1}^f = \mathbf{M}_{q+1 \leftarrow q} \mathbf{P}_q^a (\mathbf{M}_{q+1 \leftarrow q})^T + \mathbf{Q}_q, \quad (3b)$$

where \mathbf{Q}_q is the model error covariance matrix. Thereafter, no model error is considered *i.e.* \mathbf{Q} is zero.

While the Kalman filter formalism is based on simple vector algebra equations, it is not easy to understand the statistical content of the error covariances, which would require representing each covariance function and exploring their temporal evolution. Fortunately, simple diagnosis can be introduced to summarize the statistical relationship between points in the geographic domain. In turn, these diagnostics can be used as parameters of covariance models, as detailed now.

2.2 Diagnosis and modelling of covariance matrix in large dimension

In data assimilation, two diagnoses for the error covariance matrices are often introduced: the variance field, and the anisotropy of the correlation functions which corresponds to the principal axes of the spatial correlation. These diagnoses are used for the description of the forecast-error covariance matrix.

The forecast error variance field, V^f , is defined by $V^f(\mathbf{x}) = \mathbb{E}((\varepsilon^f(\mathbf{x}))^2)$ where \mathbf{x} denotes the coordinate of a grid point. The variance field also corresponds to the diagonal of \mathbf{P}^f . The field of variance characterizes the magnitude of the error at a given position.

When the forecast-error is a differential random field, the anisotropy of the correlation is characterized by the so-called local forecast-error metric tensor $\mathbf{g}^f(\mathbf{x})$ that appears in the Taylor expansion of the correlation function (Daley, 1991)

$$150 \rho^f(\mathbf{x}, \mathbf{x} + \delta\mathbf{x}) \approx 1 - \frac{1}{2} \|\delta\mathbf{x}\|_{\mathbf{g}^f(\mathbf{x})}^2, \quad (4)$$

where $\|\cdot\|_{\mathbf{g}}$ stands for the Euclidean norm associated with a metric \mathbf{g} and defined from $\|\mathbf{x}\|_{\mathbf{g}}^2 = \mathbf{x}^T \mathbf{g} \mathbf{x}$. The local metric tensor $\mathbf{g}^f(\mathbf{x})$ is a symmetric positive-definite matrix that prevents the correlation value from being larger than one. There is one local

metric tensor at each grid location \mathbf{x} . The metric tensor is related to the statistics of the random field ε^f according to the formula
 155 (Berre et al., 2007):

$$\mathbf{g}_{ij}^f(\mathbf{x}) = \mathbb{E} \left[\partial_{\mathbf{x}^i} \left(\frac{\varepsilon^f}{\sigma^f} \right) \partial_{\mathbf{x}^j} \left(\frac{\varepsilon^f}{\sigma^f} \right) \right] (\mathbf{x}), \quad (5)$$

where $\sigma^f = \sqrt{V^f}$ is the forecast-error standard deviation, and where \mathbf{x}_i 's are the coordinate functions associated with the coordinate system \mathbf{x} .

In practice, the direction of the largest correlation anisotropy corresponds to the principal axe of the smallest eigenvalue for
 160 the metric tensor: the metric tensor is *contravariant*. It is thus useful to introduce the local aspect tensor (Purser et al., 2003) whose geometry goes as the correlation, and is defined as the inverse of the metric tensor:

$$\mathbf{s}^f(\mathbf{x}) = (\mathbf{g}^f(\mathbf{x}))^{-1}, \quad (6)$$

where the superscript $^{-1}$ denotes the matrix inverse. Note that in a 1D domain, the square root of s is homogeneous to a length, leading to the so called length-scale $l = \sqrt{s}$ which is often introduced in diagnoses.

165 One of the motivations behind the diagnosis of the variance and the local anisotropy tensor is that they can be used as parameters of covariance models, the VLATcov models (Pannekoucke, 2021). For instance, for the covariance model based on a diffusion equation (Weaver and Courtier, 2001), the anisotropy tensor has been used as a proxy for setting the heterogeneous diffusion tensor field of the covariance model based on a heterogeneous diffusion equation (Pannekoucke and Massart, 2008; Mirouze and Weaver, 2010). This covariance model is used in variation data assimilation to generate heterogeneous covariances
 170 where correlation functions vary between grid points. While there is no analytical expression for the covariance functions based on the diffusion operator, analytical heterogeneous VLATcov models exist, for instance the heterogeneous Gaussian-like covariance model

$$\mathbf{P}^{\text{he.gauss}}(V, \mathbf{s})(\mathbf{x}, \mathbf{y}) = \sqrt{V(\mathbf{x})V(\mathbf{y})} \frac{|\mathbf{s}(\mathbf{x})|^{1/4} |\mathbf{s}(\mathbf{y})|^{1/4}}{|\frac{1}{2}(\mathbf{s}(\mathbf{x}) + \mathbf{s}(\mathbf{y}))|^{1/2}} \exp \left(-\frac{1}{2} \|\mathbf{x} - \mathbf{y}\|_{[\frac{1}{2}(\mathbf{s}(\mathbf{x}) + \mathbf{s}(\mathbf{y}))]^{-1}}^2 \right), \quad (7)$$

175 with $|\cdot|$ denoting the matrix determinant (Paciorek and Schervish, 2006).

Heterogeneous covariance models are important because they provide a way to produce non-obvious correlation functions from a set of parameters. Hence, approximating a covariance matrix, as the forecast-error covariance at a given time, by a covariance model is reduced to the knowledge of a set of parameters. The parametric Kalman filter takes advantage of this kind of approximation to reproduce the Kalman filter dynamics as now explained.

180 2.3 Formalism of the parametric Kalman filter

A covariance model is first considered, $\mathbf{P}(\mathcal{P})$, where \mathcal{P} denotes a set of parameters. For instance, when the PKF is designed from a VLATcov models, the set of parameters \mathcal{P} is given by the field of variance and of the local anisotropic tensors *i.e.* $\mathcal{P} = (V, \mathbf{s})$ or $\mathcal{P} = (V, \mathbf{g})$.

To describe the sequential evolution of error covariance matrices along the assimilation cycles we assume that the forecast error-covariance matrix at a time t_q , \mathbf{P}_q^f , is approximated by the covariance model, $\mathbf{P}(\mathcal{P}_q^f)$, where \mathcal{P}_q^f denotes a set of parameters so that $\mathbf{P}(\mathcal{P}_q^f) \approx \mathbf{P}_q^f$.

At an abstract level, the parametric Kalman filter consists of the following sequential steps (Pannekoucke, 2021). The PKF analysis step, equivalent to Eq. (2), consists to determine the analysis state \mathcal{X}_q^a and the parameters \mathcal{P}_q^a from \mathcal{X}_q^f , \mathcal{P}_q^f and the observations. In practice, this step consists in a sequential processing of observations, similar to the one often encountered in EnKF (Houtekamer and Mitchell, 2001), that is a sequential assimilation of single observations based on Eq. (2a) for the mean accompanied with an update of the covariance parameters so that, at the end of the analysis step, $\mathbf{P}(\mathcal{P}_q^a)$ approximates the analysis error covariance of the Kalman filter Eq. (2b) *i.e.* $\mathbf{P}(\mathcal{P}_q^a) \approx \mathbf{P}_q^a$. Note that this sequential assimilation of observations can be performed in parallel as for the EnKF, with the difference that the EnKF often assimilates a batch of observations in place of a single observation. Of course, for the PKF this step only relies on the update of the parameters, with no ensemble. For instance, when considering a VLATcov model $\mathbf{P}(V, \mathbf{s})$, the PKF analysis of a single observation at position \mathbf{x}_l , of value y^o and observation-error variance $V^o(\mathbf{x}_l)$, writes (at time t_q) (Pannekoucke, 2021)

$$\mathcal{X}^a(\mathbf{x}) = \mathcal{X}^f(\mathbf{x}) + \sigma^f(\mathbf{x}) \rho_{\mathbf{x}_l}^f(\mathbf{x}) \frac{\sigma^f(\mathbf{x}_l)}{V^f(\mathbf{x}_l) + V^o(\mathbf{x}_l)} (y^o - \mathcal{X}^f(\mathbf{x}_l)), \quad (8a)$$

$$V^a(\mathbf{x}) = V^f(\mathbf{x}) \left(1 - [\rho_{\mathbf{x}_l}^f(\mathbf{x})]^2 \frac{V^f(\mathbf{x}_l)}{V^f(\mathbf{x}_l) + V^o(\mathbf{x}_l)} \right), \quad (8b)$$

$$\mathbf{s}^a(\mathbf{x}) \approx \frac{V^a(\mathbf{x})}{V^f(\mathbf{x})} \mathbf{s}^f(\mathbf{x}), \quad (8c)$$

where the function $\rho_{\mathbf{x}_l}^f(\mathbf{x}) = \rho(\mathbf{s}^f)(\mathbf{x}_l, \mathbf{x})$ is the correlation function between the observation location and each model gridpoint \mathbf{x} , associated with the covariance matrix $\mathbf{P}(V^f, \mathbf{s}^f)$; $\sigma^f = \sqrt{V^f}$ is the field of forecast-error standard deviation; and where Eq. (8c) is the leading order approximation of the anisotropy update (Pannekoucke, 2021).

Then, the forecast step of the PKF, equivalent to Eq. (3), consists of finding the dynamics of the parameters in order to predict \mathcal{P}_{q+1}^f from \mathcal{P}_q^a , so that $\mathbf{P}(\mathcal{P}_{q+1}^f)$ approximates the forecast-error covariance matrix of the Kalman filter *i.e.* $\mathbf{P}(\mathcal{P}_{q+1}^f) \approx \mathbf{P}_{q+1}^f$. The equation for the mean is the Eq. (3a) of the KF.

2.4 PKF for advection equation of passive tracer

An illustration of the PKF is now proposed for an univariate advection problem, with a focus on the forecast step. This introduction of an intermediate problem aims to give the reader a good understanding of the PKF, its advantages and difficulties, which will be necessary to address the more complex problem encountered in multivariate CTM.

For a one-dimensional (1D) and periodic domain, of coordinate x , the conservative advection of a tracer, $\mathcal{X}(t, x)$, by a stationary heterogeneous wind field $u(x)$, can be described by the partial differential dynamics

$$\partial_t \mathcal{X} + \partial_x (u \mathcal{X}) = 0, \quad (9a)$$

or equivalently by

$$\partial_t \mathcal{X} + u \partial_x \mathcal{X} = -\mathcal{X} \partial_x u. \quad (9b)$$

215 The forecast step of the PKF is illustrated for the conservative dynamics where the covariance matrices are approximated by a VLATcov model. The computation of the PKF dynamics can be performed from using SymPKF (Pannekoucke and Arbogast, 2021), and reads as

$$\partial_t \mathcal{X} + u \partial_x \mathcal{X} = -\mathcal{X} \partial_x u, \quad (10a)$$

$$\partial_t V + u \partial_x V = -2V \partial_x u, \quad (10b)$$

220 $\partial_t s + u \partial_x s = 2s \partial_x u.$ (10c)

where here \mathcal{X} stands for the mean state $\bar{\mathcal{X}}$ and where the forecast-error upper-script $(\cdot)^f$ has been removed for V and s for the sake of simplicity. Note that the PKF system Eq. (10), which is decoupled, corresponds to the true uncertainty dynamics for the advection problem (Cohn, 1993; Pannekoucke et al., 2016, 2018). This is not true in general where closure issue can appear *e.g.* for a diffusion equation, because of the second-order derivative, an unknown term appears in the dynamics of the metric and has to be closed (Pannekoucke et al., 2018).

In the following, a numerical test-bed shows the ability of the PKF to predict the uncertainty dynamics compared to a reference ensemble estimation (EnKF).

The numerical experiment studies the time propagation of an uncertainty at time $t = 0$, featured by a mean state \mathcal{X}^0 and an error covariance \mathbf{P}^0 , to an arbitrary time T . Here, the initial error covariance is defined as the covariance $\mathbf{P}^0 = \mathbf{P}(V^0, s^0)$, where $\mathbf{P}(V, s)$ is the VLATcov model based on the heterogeneous Gaussian like model Eq. (7), for (V^0, s^0) given.

To assess the PKF ability to forecast the error statistics, we compare its results with diagnoses obtained from the forecast of a large ensemble, $\{\mathcal{X}_k^f\}_{1 \leq k \leq N_e}$, of size $N_e = 6400$, which implies a relative error of 1.25%, according to the central limit theorem. At $t = 0$, the ensemble is populated for each k as $\mathcal{X}_k^f(0) = \mathcal{X}^0 + \mathbf{P}_0^{1/2} \zeta_k$, where $\mathbf{P}_0^{1/2}$ is the square-root of the initial covariance matrix \mathbf{P}_0 , and ζ_k a Gaussian sample with zero mean and covariance matrix \mathbf{I}_n where n is the dimension of the vector \mathcal{X} *i.e.* $\zeta_k \sim \mathcal{N}(0, \mathbf{I}_n)$. Then, each member \mathcal{X}_k^f is computed from the time integration of Eq. (9b) starting from $\mathcal{X}_k^f(0)$. Note that, for the linear dynamics Eq. (9a), the full computation of the KF covariance prediction could have been considered, but the ensemble approximation has been preferred since it introduces the methodology adapted to the nonlinear setting explored for the multivariate situation in Section 3.

Hence, from the ensemble, the variance at a given time is then estimated from its unbiased estimator

240
$$\widehat{V}^f(x) = \frac{1}{N_e - 1} \sum_{k=1}^{N_e} (\varepsilon_k^f)^2, \quad (11)$$

with $\varepsilon_k^f = \mathcal{X}_k^f(x) - \widehat{\mathcal{X}}^f(x)$ and where $\widehat{\mathcal{X}}^f = \frac{1}{N_e} \sum_{k=1}^{N_e} \mathcal{X}_k^f$ is the empirical mean. The metric tensor, defined from Eq. (5), is estimated by

$$\widehat{g}^f(x) = \frac{1}{N_e} \sum_{k=1}^{N_e} (\partial_x \tilde{\varepsilon}_k^f(x))^2, \quad (12)$$

where $\tilde{\varepsilon}_k^f = \frac{1}{\sqrt{\widehat{V}^f}} (\mathcal{X}_k^f - \widehat{\mathcal{X}}^f)$ is the normalized error, and is used to compute the estimation of the aspect tensor $\widehat{s}^f(x) =$
 245 $1/\widehat{g}^f(x)$ and of the length-scale $\widehat{l}^f(x) = 1/\sqrt{\widehat{g}^f(x)} = \sqrt{\widehat{s}^f(x)}$.

The numerical framework used to forecast both the ensemble and the PKF system is now described. The periodic domain is $[0, D]$ with $D = 1000\text{km}$. It is regularly discretized with $N_x = 241$ grid points, which corresponds to a meshsize Δx of size 4.15km . The dynamics Eq. (9b) and Eq. (10) are discretized with a finite difference method, where spatial derivatives are approximated using a centred scheme of order 2. The time integration is done using a fourth-order Runge-Kutta (RK4) scheme of time step Δt verifying the Courant-Friedrichs-Lewy condition (CFL) (Weisstein, 2002) $\Delta t = \Delta x/U_{max}$, where U_{max} is the maximum wind speed magnitude of u .

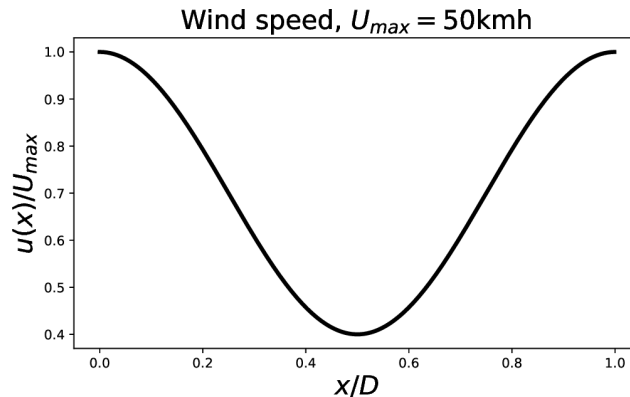


Figure 1. Predefined heterogeneous and stationary wind field $u(x)$ used for the transport simulations.

For this experiment, the mean state \mathcal{X} , the variance field V and the aspect-tensor field s are initialized homogeneously with values $\mathcal{X}^0 = 1$, $V^0 = (\sigma^0)^2$ where $\sigma^0 = 0.1$, and $s^0 = (l_h^0)^2$ where $l_h^0 = 15\Delta x \simeq 62.2\text{km}$. This initial setting also corresponds to the initial state of the PKF dynamics Eq. (10). In regards of the domain chosen, this setting for the length-scale is in agreement with practical estimations often encountered (Ménard et al., 2016). The wind field considered, shown in Fig. 1, is defined by $u(x) = (35 + 15 \cos(2\pi x))/D$, and modelizes a wind of average intensity 35kmh^{-1} and of max speed $U_{max} = 50\text{kmh}^{-1}$. The characteristic time τ_{adv} is defined by $\tau_{adv} = D/\bar{u} \simeq 28.5\text{h}$, and approximately corresponds to the time of a revolution of the tracer around the periodic domain. The simulation time horizon $T = t_{end}$ is set to $t_{end} = 3\tau_{adv}$.

The dynamics of the uncertainty shows, Fig 2, that the tracer tends to concentrate in the deceleration zones (see Fig. 1 from $x = 0$ to $x = 0.5$), and to dilute in the acceleration zones (from $x = 0.5$ to $x = 1.0$) (Fig 2(a)). This observation also applies to the standard-deviation field Fig 2(b), as it is governed by the same dynamic as the tracer's concentration (it is straightforward to calculate the dynamics of σ using the dynamics of the variance Eq. (10b)). On Fig 2(c), the length-scales (1D equivalent of the anisotropy) are subject to two processes: a pure transport term, (l.h.s. of Eq. (10c)), and a production term related to the wind sheer (r.h.s. of Eq. (10c)). This production term is positive (negative) when the wind field is accelerating (decelerating), indicating an increase (decrease) of the length-scales in the accelerating (decelerating) wind regions. In contrary to the concentrations and standard-deviation fields (governed by a conservative transport), the average value of the length-scales varies in time, however numerical experiments (not shown here) have shown that it oscillates around the initial value.

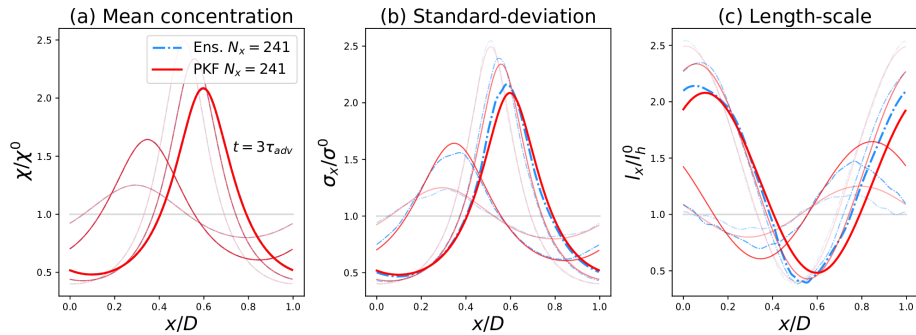


Figure 2. Comparison of the (low resolution) forecasts ($N_x = 241$) of the mean state (panel a), the forecast-error standard-deviation $\sigma = \sqrt{V}$ (panel b) and the forecast-error length-scale $l = 1/\sqrt{g} = \sqrt{s}$ (panel c), shown at times $t = [0.6, 1.2, 1.8, 2.4, 3.0]\tau_{adv}$, computed from the PKF (red lines) and compared with the diagnoses on an ensemble of $N_e = 6400$ forecasts (cyan dash-dotted lines). The more transparent the curve, the closer it is to $t = 0$. The horizontal grey lines represent the initial conditions.

Regarding the performances of the two methods, the PKF forecast results for the error statistics are quite similar to the one diagnosed from the ensemble *i.e.* the EnKF for this test-bed. The forecasts of the concentrations Fig 2(a) are identical for both methods. Although the dynamics for the variance Eq. (10b) and the anisotropy Eq. (10c) are exact in the PKF system, a significant difference is observed between the forecasts of the two methods (Fig 2(b) and Fig 2(c)). This difference is due to errors in the EnKF, rather than errors in the PKF. Note that the model error that affects the EnKF can be corrected by performing high-resolution simulations ($N_x = 723$, see Appendix A for details). This highlights some of the limitations of the numerical validation of the PKF by an ensemble method in presence of model error. This numerical experiment shows that the PKF is able to produce high quality forecasts of the diagnoses of the forecast-error statistics, a result that is confirmed by looking at the forecast-error correlation functions (see Appendix B).

This example shows the motivation behind the PKF: it is able to predict the (main parameters of the) error covariance with a good skill and at a low numerical cost. This low numerical cost first concerns the computer memory: the information contained in a covariance matrix of size $\mathcal{O}(N_x^2)$ in the ensemble case, is reduced by the covariance model Eq. (7) which only needs a few parameters of size of order $\mathcal{O}(N_x)$ (with \mathcal{O} being the Big O notation, meaning "proportional to"). But the low numerical cost concerns also the time consumed to predict the uncertainty: the PKF only relies on the single time integration of Eq. (10), that represents the cost of 3 time integrations of the initial dynamics Eq. (9b), compared to the 6400 time integrations required for the ensemble used here.

As another advantage, the PKF provides informations about the physics of the uncertainty: when ensemble diagnosis only observes the time evolution of the statistics without any explications, the PKF provides a simplified proxy that details the origin of these statistical evolutions with only three equations and by thus the PKF improves our knowledge of uncertainty dynamics.

3 Toward a multivariate formulation of the PKF

The exploration of the multivariate extension is now addressed. For multivariate problems, a modelization of the cross-correlation functions (or inter-species correlation functions) is needed. Moreover, it would be convenient to introduce a multivariate covariance model that extends the univariate VLATcov model, as the heterogeneous Gaussian model (Eq. 7), to take advantage of the PKF dynamics of univariate statistics.

Because multivariate modelling is a difficult topic, a multivariate covariance model is proposed in a simplified test-bed in Section 3.1, where a data-driven modeling is considered to determine a multivariate covariance model and its parameters. Next the multivariate PKF is formulated, detailing the prediction and the analysis steps in Section 3.2. Finally, two numerical assimilation experiments are conducted in Section 3.3

3.1 Development of a proxy multivariate covariance model

3.1.1 Introduction of the simplified chemical transport model

To explore a multivariate formulation of the PKF, a simplified chemical transport model is introduced that mimics the MOCAGE framework. This simplified CTM contains the essential features of what can be found in a more realistic CTM, that is advection, multiple chemical species and non-linearities.

To do so, a 1D periodic domain of coordinate x is considered, where two non-linearly reactive chemical species, $A(t, x)$ and $B(t, x)$, are advected in a conservative way by a heterogeneous and stationary wind field $u(x)$. The non-linear reaction is given by the Lotka-Volterra (LV) equations (see Appendix C), which leads to the coupled dynamics

$$\partial_t A + u \partial_x A = -A \partial_x u + k_1 A - k_2 AB, \quad (13a)$$

$$\partial_t B + u \partial_x B = -B \partial_x u + k_2 AB - k_3 B. \quad (13b)$$

where the transport is written following the univariate 1D example Eq. (9b), and where the LV reaction appears as the last two terms in the right hand side of each prognostic equations. The constants k_1 , k_2 and k_3 characterize the reaction rates: k_1 corresponds to the rate at which A is produced; constant k_2 represents the rate at which the chemical reactions between A and B produces $2B$; and k_3 describes the decay rate for specie B . Note that at a formal level, the state vector associated with Eq. (13) is then $\mathcal{X}(t, x) = (A, B)(t, x)$.

Considered as a dynamical system of ordinary equations and represented in the phase space (A, B) , the solutions of the Lotka-Volterra's dynamics are periodical orbits flowing around the critical point of coordinates $(A_c, B_c) = \left(\frac{k_3}{k_1}, \frac{k_1}{k_2}\right)$, as shown in Fig. 3. This is the kind of time evolution observed at each grid point when there is no wind ($u = 0$).

In this multivariate framework, the error-covariance matrix $\mathbf{P} = \mathbb{E}(\varepsilon_{\mathcal{X}}(\varepsilon_{\mathcal{X}})^T)$ associated with the state $\mathcal{X} = (A, B)$, of error $\varepsilon_{\mathcal{X}} = (\varepsilon_A, \varepsilon_B)$, reads as a block matrix

$$\mathbf{P} = \begin{pmatrix} \mathbf{P}_A & (\mathbf{P}_{AB})^T \\ \mathbf{P}_{AB} & \mathbf{P}_B \end{pmatrix}, \quad (14)$$

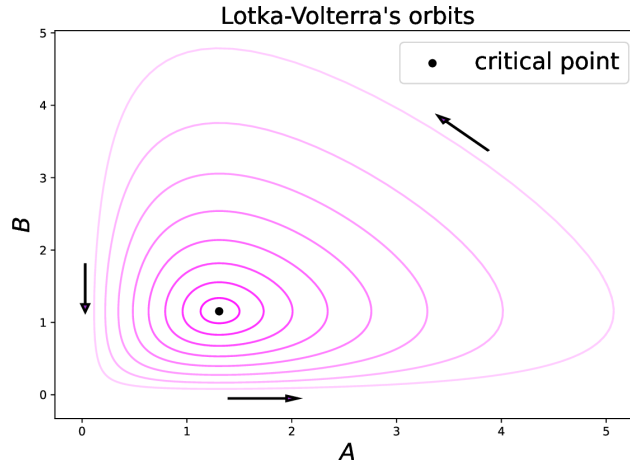


Figure 3. Numerical simulations of the Lotka-Volterra dynamical system whose solutions are periodical orbits (purple curves with different transparencies), flowing counter clockwise around the critical point $(A_c, B_c) = \left(\frac{k_3}{k_1}, \frac{k_1}{k_2}\right)$ (black dot).

where \mathbf{P}_A and \mathbf{P}_B are the autocovariance matrices of the errors, and \mathbf{P}_{AB} the cross-covariance matrix, or the inter-species covariance matrix, of the errors. Note that, in general, \mathbf{P}_{AB} is not symmetric *i.e.* $(\mathbf{P}_{AB})^T \neq \mathbf{P}_{AB}$. The two-points cross covariance function $\mathbf{P}_{AB}(x, y) = \overline{\varepsilon_A(x)\varepsilon_B(y)}$ between grid points of coordinate x and y writes

$$320 \quad \mathbf{P}_{AB}(x, y) = \sqrt{V_A(x)}\sqrt{V_B(y)}\rho_{AB}(x, y), \quad (15)$$

where

$$\rho_{AB}(x, y) = \frac{\mathbf{P}_{AB}(x, y)}{\sqrt{V_A(x)}\sqrt{V_B(y)}}, \quad (16)$$

is the cross-correlation function. The cross-correlation function is not symmetric in general *i.e.* $\rho_{AB}(x, y) \neq \rho_{AB}(y, x)$. In particular, if \mathbf{C}_{AB} denotes the associated cross-correlation matrix, then $\mathbf{C}_{AB} \neq (\mathbf{C}_{AB})^T$.

325 At a covariance modelling point of view, and in the perspective of the PKF, the univariate covariances \mathbf{P}_A and \mathbf{P}_B could be approximated by a VLATcov model *e.g.* $\mathbf{P}(V_A, s_A)$. Moreover, the single-point cross-covariance field defined as $V_{AB}(x) = \overline{\varepsilon_A(x)\varepsilon_B(x)}$ will appear in the dynamics of V_A and V_B because of the coupling due to LV equations, and should be considered as a natural parameter for a multivariate PKF. At this stage, the question is whether it is possible to approximate the two-points cross-covariance functions $\mathbf{P}_{AB}(x, y)$ knowing the parameters $(\bar{A}, \bar{B}, V_A, V_B, V_{AB}, s_A, s_B)$ which are functions of x .

330 Since no multivariate modelling extending the VLATcov model is available. A numerical exploration of the dynamics of multivariate statistics is performed for the LV-CTM, so then to guess a proxy for the cross-covariance functions.

3.1.2 Ensemble of multivariate forecasts

Compared to the univariate experiment described in Section 2.4, without a multivariate covariance model, it is not possible to sample a multivariate ensemble. For this reason, the error for the two chemical species are assumed decorrelated at the initial

335 time $t = 0$, so that the error-covariance matrix, \mathbf{P}^0 , is the block diagonal

$$\mathbf{P}^0 = \begin{pmatrix} \mathbf{P}_A^0 & 0 \\ 0 & \mathbf{P}_B^0 \end{pmatrix}, \quad (17)$$

where \mathbf{P}_A^0 (\mathbf{P}_B^0) is the univariate covariance associated with error on A (B). Following the ensemble generation of Section 2.4, the univariate covariance matrices are chosen as the two VLATcov $\mathbf{P}_A^0 = \mathbf{P}(V_A^0, s_A^0)$ and $\mathbf{P}_B^0 = \mathbf{P}(V_B^0, s_B^0)$. Then, an ensemble of $N_e = 6400$ initial conditions $(\mathcal{X}_k^0)_{k \in [1, N_e]}$ is sampled, with for each k , $\mathcal{X}_k^0 = \mathcal{X}^0 + (\mathbf{P}^0)^{1/2} \zeta_k$, where $\mathcal{X}^0 = (A^0, B^0)$ and
 340 $(\mathbf{P}^0)^{1/2}$ is the block diagonal matrix $(\mathbf{P}^0)^{1/2} = \text{diag}(\mathbf{P}(V_A^0, s_A^0)^{1/2}, \mathbf{P}(V_B^0, s_B^0)^{1/2})$. This time, ζ_k is a sample of $\mathcal{N}(0, \mathbf{I}_n)$ with $n = 2N_x$. The domain is discretized in $N_x = 723$ grid points.

For the simulation, the fields A^0 and B^0 are set to the constants $A^0 = 1.2$ and $B^0 = 0.8$. The univariate parameters are set to $\sigma_A^0 = 0.1 \cdot A^0$, $\sigma_B^0 = 0.1 \cdot B^0$, $s_A^0 = s_A^0 = l_h^2$ with $l_h = 45\Delta x \simeq 62\text{km}$. The reaction rates of LV are set to $(k_1, k_2, k_3) = (0.075, 0.065, 0.085)$. The time integration follows the numerical setting used for the univariate simulation presented in Sec-
 345 tion 2.4, and leads to an ensemble of $N_e = 6400$ multivariate forecasts.

While there is no cross-correlation at the initial condition, the coupling provided by the LV equations should introduce a non-zero cross-correlation between errors on A and B , and this can be diagnosed from the computation of the ensemble estimation of the two-points forecast-error cross-covariance function $\mathbf{P}_{AB}(x, y)$ at time t , given by

$$\widehat{\mathbf{P}}_{AB}(t, x, y) = \frac{1}{N_e - 1} \sum_{k=1}^{N_e} \varepsilon_{A,k}(t, x) \varepsilon_{B,k}(t, y), \quad (18)$$

350 with $\varepsilon_{A,k}(t, x) = A_k(t, x) - \widehat{A}(t, x)$ and $\varepsilon_{B,k}(t, y) = B_k(t, y) - \widehat{B}(t, y)$, where \widehat{A} and \widehat{B} are the empirical means of the ensemble of forecasts (A_k) and (B_k), from which an estimation of the cross-correlation functions $\widehat{\rho}_{AB}(t, x, y)$ and matrix $\widehat{\mathbf{C}}_{AB}(t)$ can be deduced.

Figure 4 shows the time evolution of the cross-correlation with respect to the grid point $x_l = 0.5$ *i.e.* the function $\rho_{AB}(x_l, \cdot)$. As it has been specified, the cross-correlation is zero at $t = 0$ (Fig. 4(a)). Then, as it is expected, the cross-correlation evolves
 355 along the time, presenting an anti cross-correlation at $t = 0.6\tau_{adv}$ (Fig. 4(b)), then a positive one at $t = 1.8\tau_{adv}$ (Fig. 4(d)). At $t = 2.4\tau_{adv}$ (Fig. 4(e)), the cross-correlation appears clearly asymmetric, while reaching its maximum value at a y strictly lower than x_l .

3.1.3 Formulation of a proxy for the cross-correlation

Now, a proxy for the cross-correlation is introduced from the data set of multivariate forecasts.

360 After a trial-and-error process, and inspired from the VLATcov model Eq. (7), the following expression

$$r_{AB}(\mathbf{x}, \mathbf{y}) = \frac{1}{2} \left(\frac{V_{AB}(\mathbf{x})}{\sigma_A(\mathbf{x})\sigma_B(\mathbf{x})} + \frac{V_{AB}(\mathbf{y})}{\sigma_A(\mathbf{y})\sigma_B(\mathbf{y})} \right) \exp \left(-\|\mathbf{x} - \mathbf{y}\|_{[\frac{1}{4}(s_A(\mathbf{x})+s_B(\mathbf{x})+s_A(\mathbf{y})+s_B(\mathbf{y}))]}^2}^{-1} \right), \quad (19)$$

as function of the known parameters $\mathcal{P} = (V_A, V_B, V_{AB}, s_A, s_B)$, has been proposed as a proxy for the cross-correlation ρ_{AB} *i.e.* $r_{AB}(x, y) \approx \rho_{AB}(x, y)$. It consists in an interpolation by the mean of the cross-correlation values at location \mathbf{x} and \mathbf{y} ,

Cross-correlation functions modelization

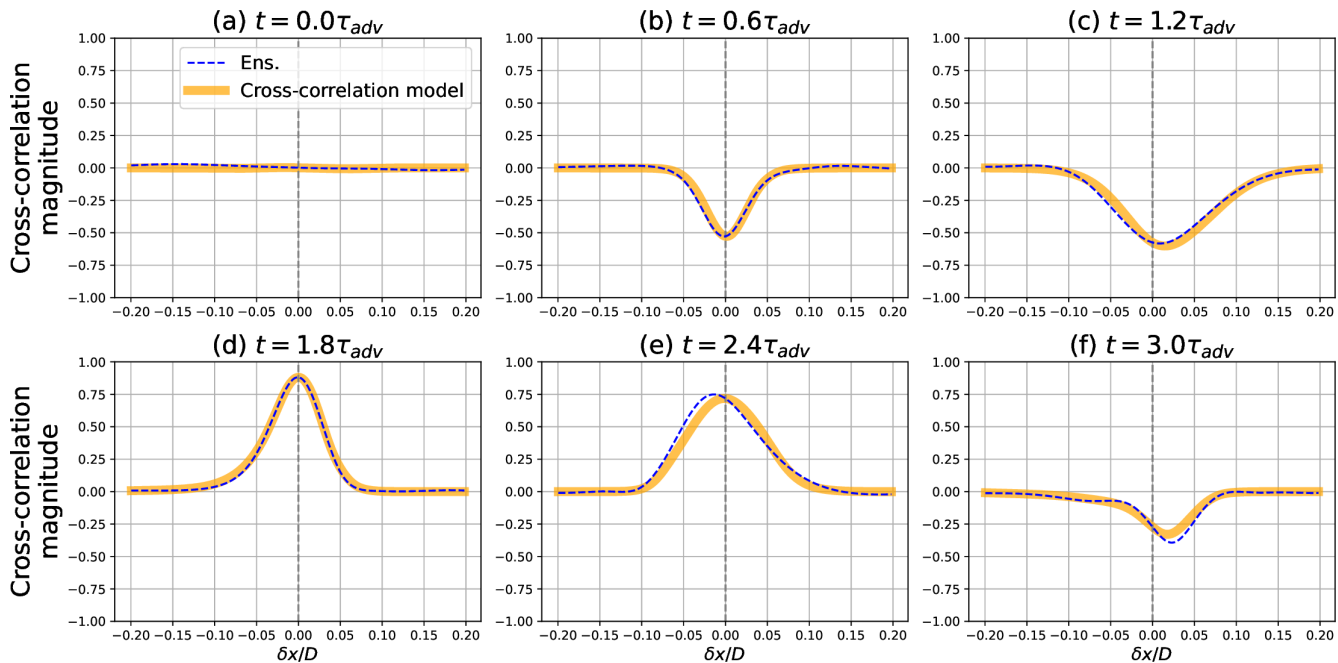


Figure 4. Evaluation of the cross-correlation model $r_{AB}(x_L, \cdot)$ (bold orange line) versus the ensemble estimation of the cross-correlation $\rho_{AB}(x_L, \cdot)$ (blue dashed line) with respect to the location $x_l = 0.5$ and times $t = [0.0, 0.6, 1.2, 1.8, 2.4, 3.0]\tau_{adv}$.

365 multiplied by a gaussian kernel, where the univariate aspect-tensor has been substituted by the mean of the aspect-tensors of all chemical species. The resulting proxy for the cross-correlation matrix is denoted by $\mathbf{C}_{AB}^{\text{proxy}}(\mathcal{P})$.

One of the main advantages of considering a simple analytic formula is its can be extended to a problem with more chemical species and for a domain of higher dimension.

Note that formulation Eq. (19) is symmetric ($r_{AB}(x, y) = r_{AB}(y, x)$), while cross-correlations are not symmetric in general
 370 ($\rho_{AB}(x, y) \neq \rho_{AB}(y, x)$), but this expression leverages on all the parameters known at locations \mathbf{x} and \mathbf{y} . However, the function $r_{AB,x}(\delta x) = r_{AB}(x, x + \delta x)$ is not necessarily symmetric in δx , where in general $r_{AB,x}(\delta x) \neq r_{AB,x}(-\delta x)$.

To assess the skill of the proxy, Fig. 4 shows the functions $r_{AB}(x_l, \cdot)$ (computed from Eq. (19) with the ensemble-estimated parameters $\hat{\mathcal{P}}(t) = (\widehat{V}_A, \widehat{V}_B, \widehat{V}_{AB}, \widehat{s}_A, \widehat{s}_B)(t)$), compared with the ensemble estimated cross-correlation $\rho_{AB}(x_l, \cdot)$. At a qualitative level, the functions r_{AB} are in accordance with the cross-correlation ρ_{AB} of reference for all the panels. Note that, while
 375 r_{AB} is symmetric, the functions $r_{AB}(x_l, \cdot)$ can be asymmetric as it appears in Fig. 4(c) and Fig. 4(f).

At a quantitative level, Fig. 5 shows the time evolution of the relative error $\frac{\|\widehat{\mathbf{C}}_{AB}(t) - \mathbf{C}_{AB}^{\text{proxy}}(\hat{\mathcal{P}}(t))\|}{\|\widehat{\mathbf{C}}_{AB}(t)\|}$, where $\|\mathbf{U}\| = \sqrt{\text{Tr}(\mathbf{U}\mathbf{U}^T)}$ is the Frobenius matrix norm where Tr is the trace operator; $\widehat{\mathbf{C}}_{AB}(t)$ is the ensemble estimation of the cross-correlation matrix; and $\mathbf{C}_{AB}^{\text{proxy}}(\hat{\mathcal{P}}(t))$ is the proxy for the cross-correlation matrix fitted with ensemble-estimated parameters $\hat{\mathcal{P}}(t)$. Two differ-

Time evolution of the relative error for the modelled cross-correlation matrix,
for identical and different initial length-scales

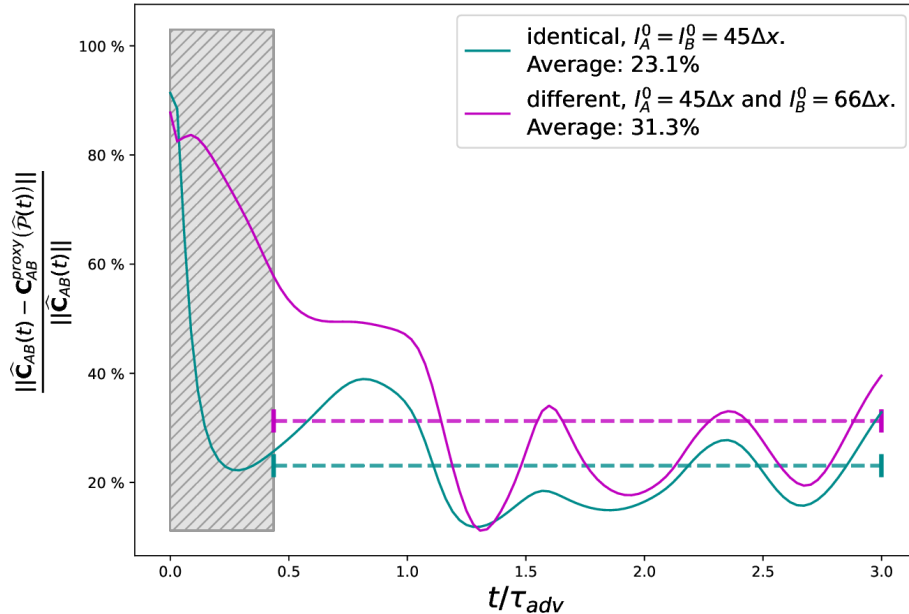


Figure 5. Time evolutions of the relative errors between the empirical cross-correlation matrix (EnKF) and the proxy-generated cross-correlation matrix fitted with EnKF-diagnosed parameters, for two different settings of the initial length scales: equal length-scales with $l_A^0 = l_B^0 = 45\Delta x \approx 66\text{km}$ (turquoise line) and different length-scales with $l_A^0 = 45\Delta x$ and $l_B^0 = 66\Delta x \approx 91\text{km}$ (mauve line). The results being dominated by sampling noise for $t < 0.45$, they are not retained (grey hatching) for the computing of the temporal averages (dashed segments).

ent experiments are shown depending on whether the initial length-scale for a A and B are equal, $l_A^0 = l_B^0 = 45\Delta x \approx 66\text{km}$ (turquoise lines) ; or different, $l_A^0 \approx 66\text{km}$ but $l_B^0 = 66\Delta x \approx 91\text{km}$ (purple lines).

As the two multivariate error fields are uncorrelated at the initial time, the true cross-correlation matrix $\mathbf{C}_{AB}(t=0)$ is zero. However, the ensemble used in the estimation of $\widehat{\mathbf{C}}_{AB}(t=0)$ being finite, this produces spurious non-zero cross-correlation leading to a non-zero matrix and to a relative error larger than 80%. Then, the first instants of the simulation are dominated by the sampling noise, and they are excluded for the analysis of the results (grey hatching). After $t \simeq 0.45$, the experiments offer valid results and lead to temporal averages of 23.1% when $l_A^0 = l_B^0$ (turquoise dashed line) and 31.3% when $l_A^0 \neq l_B^0$. Note that the effect of the sampling noise can leads to an overestimation of 8% for this kind of experiment (Pannekoucke, 2021).

According to our knowledge, no proxy of cross-correlations similar to Eq. (19) has been introduced up to now as a possible proxy of cross-correlations. As mentioned above, r_{AB} does not share the same property of the cross-correlation (*e.g.* r_{AB} is symmetric while ρ_{AB} is not), and thus, there is no guarantee that a multivariate covariance model based on the proxy r_{AB} leads to a true covariance matrix: such a multivariate covariance model is symmetric because r_{AB} is symmetric, but not necessarily positive definite, although it may not be essential for the PKF applications.

Despite of the limitations of the proxy, a multivariate extension of the univariate VLATcov model is explored below, where the cross-correlation is approximated by the proxy Eq. (19). This leads to a multivariate VLATcov model of parameters the fields $(V_{AB}, V_A, V_B, s_A, s_B)$ for which we can formulate a PKF.

395 3.2 Formulation and simplification of the parameters dynamics and analysis

3.2.1 PKF dynamics for LV-CTM

The computation of the PKF dynamics leverages on the SymPKF package which applied to the dynamics Eq. (13), provides the following system of coupled equations

$$\partial_t A + u \partial_x A = -A \partial_x u + k_1 A - k_2 AB - k_2 V_{AB} \quad (20a)$$

$$400 \quad \partial_t B + u \partial_x B = -B \partial_x u - k_3 B + k_2 AB + k_2 V_{AB} \quad (20b)$$

$$\partial_t V_{AB} + u \partial_x V_{AB} = -2V_{AB} \partial_x u + V_{AB}(k_1 - k_2 B - k_3 + k_2 A) + k_2 V_A B - k_2 V_B A \quad (20c)$$

$$\partial_t V_A + u \partial_x V_A = -2V_A \partial_x u + 2[V_A(k_1 - k_2 B) - k_2 A V_{AB}] \quad (20d)$$

$$\partial_t V_B + u \partial_x V_B = -2V_B \partial_x u + 2[V_B(-k_3 + k_2 A) + k_2 B V_{AB}] \quad (20e)$$

$$405 \quad \begin{aligned} \partial_t s_A + \underbrace{u \partial_x s_A}_{T_{A,adv-1}} &= \underbrace{2s_A \partial_x u}_{T_{A,adv-2}} - \underbrace{\frac{2k_2 A V_{AB} s_A}{V_A}}_{T_{A,chem-1}} + \underbrace{\frac{2k_2 A \sigma_B s_A^2 \overline{\partial_x \tilde{\varepsilon}_A} \overline{\partial_x \tilde{\varepsilon}_B}}{\sigma_A}}_{T_{A,chem-2}} \\ &+ \underbrace{\frac{k_2 A s_A^2 \overline{\tilde{\varepsilon}_B} \overline{\partial_x \tilde{\varepsilon}_A} \overline{\partial_x V_B}}{\sigma_A \sigma_B}}_{T_{A,chem-3}} - \underbrace{\frac{k_2 A \sigma_B s_A^2 \overline{\tilde{\varepsilon}_B} \overline{\partial_x \tilde{\varepsilon}_A} \overline{\partial_x V_B}}{V_A^{\frac{3}{2}}}}_{T_{A,chem-4}} + \underbrace{\frac{2k_2 \sigma_B s_A^2 \overline{\tilde{\varepsilon}_B} \overline{\partial_x \tilde{\varepsilon}_A} \overline{\partial_x A}}{\sigma_A}}_{T_{A,chem-5}} \end{aligned} \quad (20f)$$

$$\begin{aligned} \partial_t s_B + \underbrace{u \partial_x s_B}_{T_{B,adv-1}} &= \underbrace{2s_B \partial_x u}_{T_{B,adv-2}} + \underbrace{\frac{2k_2 B V_{AB} s_B}{V_B}}_{T_{B,chem-1}} - \underbrace{\frac{2k_2 B \sigma_A s_B^2 \overline{\partial_x \tilde{\varepsilon}_A} \overline{\partial_x \tilde{\varepsilon}_B}}{\sigma_B}}_{T_{B,chem-2}} \\ &- \underbrace{\frac{k_2 B s_B^2 \overline{\tilde{\varepsilon}_A} \overline{\partial_x \tilde{\varepsilon}_B} \overline{\partial_x V_A}}{\sigma_A \sigma_B}}_{T_{B,chem-3}} + \underbrace{\frac{k_2 B \sigma_A s_B^2 \overline{\tilde{\varepsilon}_A} \overline{\partial_x \tilde{\varepsilon}_B} \overline{\partial_x V_B}}{V_B^{\frac{3}{2}}}}_{T_{B,chem-4}} - \underbrace{\frac{2k_2 s_B^2 \overline{\tilde{\varepsilon}_A} \overline{\partial_x \tilde{\varepsilon}_B} \overline{\partial_x B}}{\sigma_B}}_{T_{B,chem-5}} \end{aligned} \quad (20g)$$

where the overline of the mean states \overline{A} and \overline{B} have been discarded for the sake of simplicity. The PKF is a second order filter in which the variance of the fluctuations modify the time evolution of the mean states *e.g.* by the term $-k_2 V_{AB}$ of Eq. (20a).

410 For the dynamics of the anisotropy, Eq. (20f) and Eq. (20g), the contributions due to the transport (to the chemistry) are labeled as $T_{(\cdot),adv-(\cdot)}$ ($T_{(\cdot),chem-(\cdot)}$) to be identified.

Note that the dynamics induced by the transport process is exact as mentioned in Sec. 2.4. In the PKF system Eq. (20) the dynamics of the mean concentrations A and B , variances V_A and V_B and cross-covariance V_{AB} , Eq. (20a) to Eq. (20e), are independent of anisotropy field Eq. (20f) and Eq. (20g). The reciprocal is not true: the anisotropy fields dynamics (Eq. (20f)-

415 Eq. (20g)) are forced by the means, the variances, the cross-covariances and their spatial heterogeneity. Eq. (20a) and Eq. (20b) also indicate an interaction between the cross-covariance and the mean concentrations.

The dynamics of the aspect tensors, Eq. (20f) and Eq. (20g), are not closed: some terms are expressed as expectations of the normalized errors $\tilde{\varepsilon}_A = \varepsilon_A/\sqrt{V_A}$ and $\tilde{\varepsilon}_B = \varepsilon_B/\sqrt{V_B}$. These open terms can not be directly expressed using the available parameters, preventing the forecast of the error statistics.

420 3.2.2 Closure of the PKF dynamics

A closure is proposed for the LV-CTM multivariate PKF dynamics. Note that the open terms of the PKF dynamics Eq. (20) can be related to spatial derivatives of the cross-correlation Eq. (16) *e.g.* $\overline{\tilde{\varepsilon}_A \partial_x \tilde{\varepsilon}_B}(x) = (\partial_x \rho_{AB})(x, x)$ or $\overline{\partial_x \tilde{\varepsilon}_A \partial_x \tilde{\varepsilon}_B}(x) = (\partial_{xy} \rho_{AB})(x, x)$, leading to a closure of the PKF dynamics when the proxy r_{AB} Eq. (19) is used in place of the true cross-correlation ρ_{AB} . However, numerical investigation of this closure did not lead to good results (not shown here).

425 From a detailed quantification of the impact of the chemistry alone (see Appendix D1) and of the relative contributions comparing the importance of the advection versus the chemistry (see Appendix D2), it results that the advection contributes to 80% of the anisotropy dynamics while 20% are due to the chemistry. Since the advection mainly leads the dynamics of the anisotropy, this suggests to remove the contribution of the chemistry in Eq. (20f) and Eq. (20g), which leads to a closure of the PKF dynamics Eq. (20) as

$$430 \quad \partial_t A + u \partial_x A = -A \partial_x u + k_1 A - k_2 AB - k_2 V_{AB} \quad (21a)$$

$$\partial_t B + u \partial_x B = -B \partial_x u - k_3 B + k_2 AB + k_2 V_{AB} \quad (21b)$$

$$\partial_t V_{AB} + u \partial_x V_{AB} = -2V_{AB} \partial_x u + V_{AB}(k_1 - k_2 B - k_3 + k_2 A) + k_2 V_{AB} - k_2 V_B A \quad (21c)$$

$$\partial_t V_A + u \partial_x V_A = -2V_A \partial_x u + 2[V_A(k_1 - k_2 B) - k_2 A V_{AB}] \quad (21d)$$

$$\partial_t V_B + u \partial_x V_B = -2V_B \partial_x u + 2[V_B(-k_3 + k_2 A) + k_2 B V_{AB}] \quad (21e)$$

$$435 \quad \partial_t s_A = -u \partial_x s_A + 2s_A \partial_x u \quad (21f)$$

$$\partial_t s_B = -u \partial_x s_B + 2s_B \partial_x u \quad (21g)$$

3.2.3 Extension of the PKF *analysis* step for multivariate assimilations

For multivariate statistics, the update Eq. (8) presented in Section 2 have to be modified: they can be applied to update the univariate error statistics (mean concentrations, variances, aspect-tensors) but do not indicate how to update the cross-covariance fields. To apply the formulas Eqs. (8) in multivariate contexts, the x_l must refer to the observation of a species Z_l at observation location, while \mathbf{x} refers to any species at any location.

For an observation at location \mathbf{x}_l of the chemical species Z_l , the cross-covariance field between two species Z_1 and Z_2 updates (see Appendix F):

$$V_{Z_1 Z_2}^a(\mathbf{x}) = V_{Z_1 Z_2}^f(\mathbf{x}) - \left(\sigma_{Z_2}^f(\mathbf{x}) \rho_{Z_2 Z_l, l}^f(\mathbf{x}) \sigma_{Z_1}^f(\mathbf{x}) \rho_{Z_1 Z_l, l}^f(\mathbf{x}) \right) \frac{V_{Z_l}^f(\mathbf{x}_l)}{V_{Z_l}^f(\mathbf{x}_l) + V_{Z_l}^o(\mathbf{x}_l)}, \quad (22)$$

where $\rho_{Z_i Z_l, l}^f(\mathbf{x})$ is the forecast cross-correlation function between Z_l and Z_i at location \mathbf{x}_l , defined by

$$\rho_{Z_i Z_l, l}^f(\mathbf{x}) = \mathbb{E} \left[\varepsilon_{Z_l}^f(\mathbf{x}_l) \varepsilon_{Z_i}^f(\mathbf{x}) \right] / \left(\sigma_{Z_l}^f(\mathbf{x}_l) \sigma_{Z_i}^f(\mathbf{x}) \right). \quad (23)$$

Note that Eq. (22) also applies when one of the two chemical species Z_1 or Z_2 coincides with Z_l . This leads to a new formulation of the algorithm PKFO1 (given by the alg. 1 in Appendix F).

450 3.3 Numerical experiments: simple forecast and data assimilation over several cycles

In this section, two numerical experiments, labeled FCST and DA, are proposed to evaluate the multivariate formulation of the PKF for the LV-CTM. Again, a large EnKF will be used as a reference to be compared with regarding the error statistics produced. The first experiment, FCST, focuses on the forecast step alone. Therefore, the PKF dynamics (Eq. (21)) and the EnKF for equations (Eq. (13)) are forecasted. Then, in DA, 5 complete data assimilation cycles are performed to test the
 455 PKF capacity to produce multivariate analysis. DA only differs from FCST by the assimilations of observations, otherwise the configurations are identical. The next section details the setup of the experiments.

3.3.1 Settings of the numerical experiments

In both experiments, the EnKF relies on 6400 members. The total time of the simulation is $t_{max} = 5\tau_{adv}/3 \simeq 47.5$ hours (τ_{adv} is the characteristic time defined in section 2.4). A high resolution with $N_x = 723$ grid points is used. The settings of the wind
 460 field, chemical rates, initial concentrations, initial variances and cross-covariance, time scheme, space grid etc. are identical to those used in section 3.1.2. The initial length-scale fields are homogeneously initialized at $l_A^0 = l_B^0 = 45\Delta x$.

For the data assimilation experiment, a network of 4 sensors regularly spaced on the right hand side of the domain is considered to generate observations of the chemical species A . Each $\tau_{adv}/3$ hours, observations are generated from an independent nature run and assimilated for both filters. The nature run is initialized with fields concentrations A and B set
 465 respectively to $1.2 + 0.12\zeta_A$ and $0.8 + 0.08\zeta_B$, where ζ_A and ζ_B are structured Gaussian random field of zero mean, standard-deviation 1 and length-scale $45\Delta x$ (*i.e.* sampled from $\mathbf{P}(1, (45\Delta x)^2)$ in Eq. (7)). The synthetic observations are considered uncorrelated in space and time (*i.e.* at a given time \mathbf{R} is diagonal), and generated at the analysis time t_a according to: $A^{obs}(x_l, t_a) = A_{NR}^f(x_l, t_a) + \sigma^{obs} \zeta_{t_a}$, where $\sigma^{obs} = 10\%$ is the observations standard-deviation, ζ_{t_a} is a sample from the standard Gaussian distribution, and A_{NR}^f is the forecast of the nature run for location x_l . The model error is neglected in this
 470 experiment (*i.e.* $\mathbf{Q} = \mathbf{0}$ in Eq. 3b). For the PKF, the observations are assimilated using the PKF O1 algorithm.

3.3.2 Results

The results for the FCST experiment are shown in Fig. 6. The figure presents the state vector (Fig. 6(a) and Fig. 6(b)) and five error statistics (Fig. 6 panels (c)-(g)) for the EnKF and the PKF at $t = 0.5t_{max}$ and $t = t_{max}$. The error statistics presented

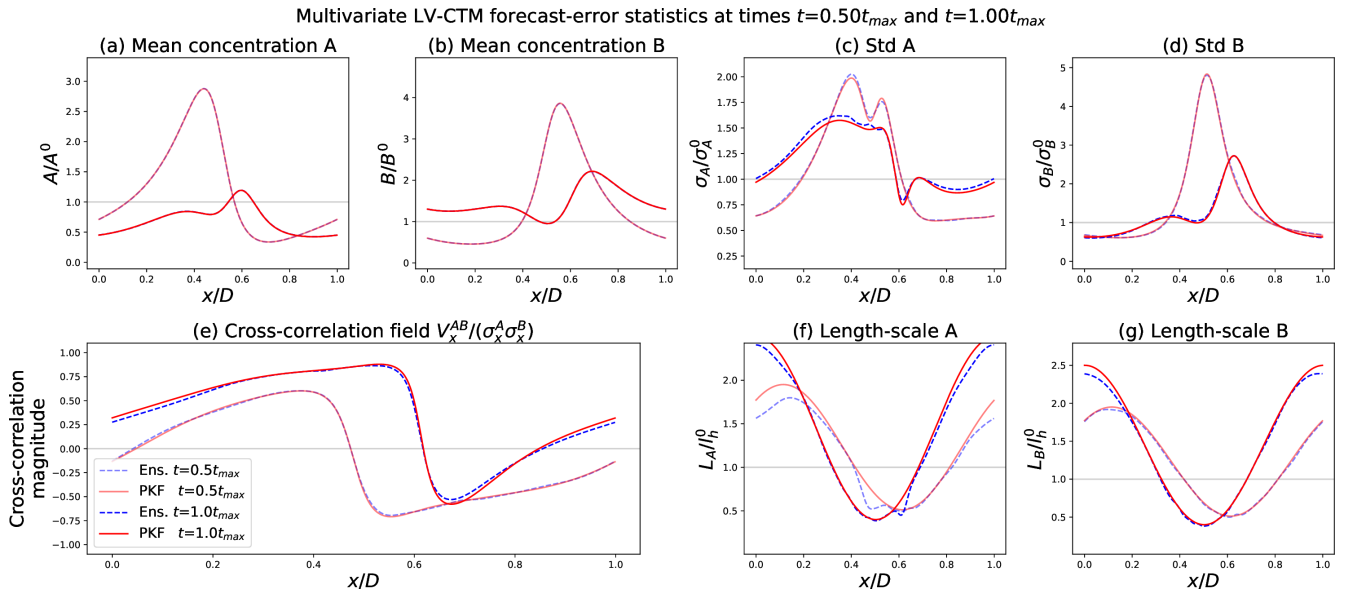


Figure 6. Results of the forecast numerical experiment. PKF errors statistics (solid red lines) and EnKF diagnosed error statistics (dashed blue lines) at times $t = [0.50, 1.00]t_{max}$. These times correspond approximately to $t=23\text{h}45\text{min}$ and $t=47\text{h}40\text{min}$.

are, from panel Fig. 6(c) to Fig. 6(g), the two standard-deviations, the cross-correlation field and the two length-scales, rather than the raw PKF parameters. A horizontal grey line on each panel is here to represent the initial setting of the corresponding quantity.

The forecasts of the means match perfectly for both methods (see Fig. 6(a) and Fig. 6(b)). Similarly to the univariate advection experiment (section 2.4, see Fig 2), an accumulation of the tracers is observed in the low wind speeds region (center of the domain). The standard-deviations (panels Fig. 6(c)-(d)) observe a similar behaviour although the effects of the chemistry appear more clearly: the curves show some quite localized deformations, especially for the standard deviation of A (compare with Fig 2(b)). The cross-correlation field Fig. 6(e), specific to the multivariate case, is predicted with great accuracy by the PKF dynamics. It indicates that, starting from decorrelated error fields for A and B , the chemistry dynamic has allowed non-zero cross-correlations to emerge by coupling the chemical species, in a non-linear fashion. While being less accurate than for the means, the filters coincide at estimating the standard-deviation as well as for the cross-correlation fields. The forecasts of the length-scales (Fig. 6(f) and (g)) show a general accordance between the two methods, even though a difference can be observed in A 's case Fig. 6(f). This gap is due to the simplification of the anisotropy dynamics in the PKF formulation Eqs. (21), which does not permit to represent such behaviours. The equation of the anisotropy dynamics of A in the original formulation of the PKF Eq. (20f) suggests an explanation to the spikes presented on the EnKF curves on Fig. 6(f) which are absent for the PKF. The terms labeled $T_{A,chem-3}$ and $T_{A,chem-4}$ indicate a forcing of the spatial derivatives of the variance V_A . Looking at Fig. 6(c), it appears that the variance of A presents some strong spatial heterogeneity ($x = 0.45$ for $t = 0.5t_{max}$, and $x = 0.60$ for $t = t_{max}$), causing important magnitudes for $\partial_x V_A$ and thus for $T_{A,chem-3}$ and $T_{A,chem-4}$. This produces a local

deformation on A 's length-scales which is effectively observed for the same times and locations on Fig. 6(f). However, these gaps between the EnKF and PKF curves are local and of a reasonable magnitude: overall, the PKF forecast for the anisotropy reproduces the EnKF results.

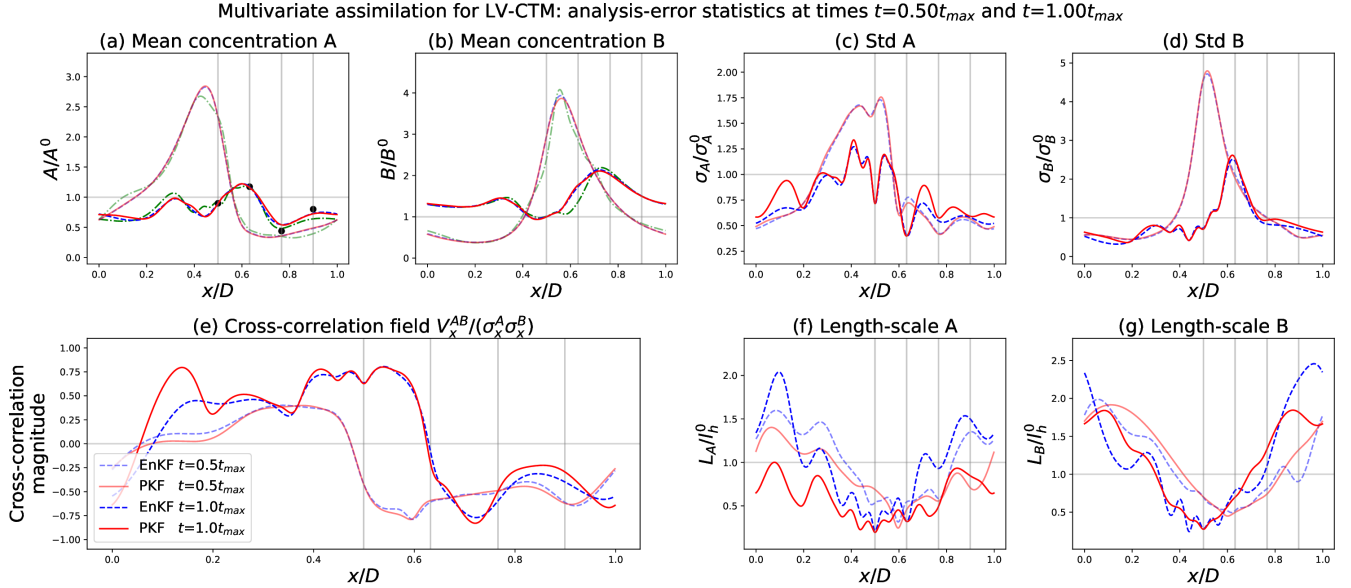


Figure 7. Results of the data assimilation numerical experiment. Nature run (dash dotted green lines, only on panels (a) and (b)), PKF errors statistics (solid red lines) and EnKF diagnosed error statistics (dashed blue lines) at times $t = [0.50, 1.00]t_{max}$. These times correspond approximately to $t=23\text{h}45\text{min}$ and $t=47\text{h}40\text{min}$. At time $t = 0.5t_{max}$, two analysis steps have already been performed. At time $t = 1.00t_{max}$, the fifth analysis step is being realized, the generated observations are represented by black dots on panel (a). The vertical grey lines correspond to the sensors locations.

495 The outcome of the DA experiment Fig. 7 is now exposed, where five assimilation cycles are done over the period $[0, t_{max}]$ (one assimilation after each $\tau_{adv}/3$ time integration, with $t_{max} = 5\tau_{adv}/3$). The results are presented similarly to the FCST experiment, except four vertical grey lines have been added to indicate the sensors locations. Also, time $t = t_{max}$ corresponds to a time for which synthetic observations for A are generated (see Fig. 7(a)).

For the DA experiment (Fig. 7), the resulting means on Fig. 7(a) and Fig. 7(b) are identical for the PKF and EnKF. This 500 indicates similar forecasts and analysis for both methods during the five assimilation cycles. However, the corrections brought by the observations are not very significant given the neglected model error, the small amplitude of the forecast variance and the observation error. This configuration implied the generated observations to be very close to the forecasted concentrations, therefore the means are not significantly different than in the FCST experiment. The impact of the different analysis is more visible on the rest of the error statistics. For instance, the standard deviation of species A Fig. 7(c) presents important down- 505 spikes which result from the uncertainty reduction during the analysis. This reduction of the uncertainty is also visible, with a reduced amplitude, on specie B Fig. 7(d) for which we do not have observations. The ability to reduce the uncertainty of B

and to correct its concentration when A is observed is the signature of the multivariate character of the analysis. The amplitude of the reduction of σ_B and correction of B is related to the strength of the cross-correlation at the moment of assimilation. The cross-correlation field Fig. 7(e) is also impacted by the observation but it is less obvious to say in which manner. Looking at Fig. 7(f), an important gap between the PKF and EnKF for the length-scales of A can be observed. It is caused by two reasons, the major one being the approximation in the anisotropy update formula Eq. (8c). This simplified formula is less accurate than its second order version Eq. (10) from Pannekoucke (2021), but offers more robustness during numerical simulations (see panel (e) of Fig. 13 from Pannekoucke (2021) and the discussion in their section 4.4). The second reason is the reduction of the anisotropy dynamics to the transport process in the PKF formulation (compare Section 3.2). Compared to the FCST experiment, the assimilation of observations has had the effect of reducing the length-scales.

In both of these experiments, the PKF has shown itself able to reproduce the results of a large ensemble Kalman Filter. Again, these qualitative results of the PKF were obtained at a low numerical cost: the equivalent of 3 time integrations of Eq. (13) compared to 6400 for the EnKF.

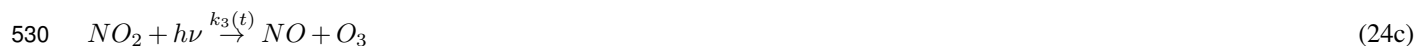
It would be interesting to assess the robustness of the results, including whether the advection terms remain dominant under different conditions, such as weaker winds or accelerated chemistry, from a set of operational CTM predictions.

4 A more realistic chemical model: the generic reaction set (GRS) model

The simplified LV-CTM has allowed for a multivariate PKF assimilation, validated in numerical experiments. To explore the ability of the PKF to apply to a more complex chemical scheme, an intermediate chemical model is now introduced, the generic reaction set (Azzi et al., 1992; Haussaire and Bocquet, 2016) (GRS), then used to validate the PKF forecast.

4.1 Description of the GRS model

GRS describes the dynamics of a reduced number of chemical species or *pseudo*-species. Hence, six species are considered and interact as



where ROC, RP and S(N)GN respectively mean *Reactive Organic Compound*, *Radical Pool* et *Stable (Non-) Gaseous Nitrogen product*. In this chemical model, additional processes such as photolysis rate variation, ground deposits or atmospheric emissions of certain pollutants are represented.

The system of equations of the GRS-CTM writes:

$$\partial_t[ROC] = -\partial_x(u \cdot [ROC]) - \lambda[ROC] + E_{ROC} \quad (25a)$$

$$\partial_t[RP] = -\partial_x(u \cdot [RP]) - \lambda[RP] + k_1(t)[ROC] - [RP](k_2[NO] + 2k_6[NO_2] + k_5[RP]) \quad (25b)$$

$$540 \quad \partial_t[NO] = -\partial_x(u \cdot [NO]) - \lambda[NO] + E_{NO} + k_3(t)[NO_2] - [NO](k_2[RP] + k_4[O_3]) \quad (25c)$$

$$\partial_t[NO_2] = -\partial_x(u \cdot [NO_2]) - \lambda[NO_2] + E_{NO_2} + k_4[NO][O_3] + k_2[NO][RP] - [NO_2](k_3(t) + 2k_6[RP]) \quad (25d)$$

$$\partial_t[O_3] = -\partial_x(u \cdot [O_3]) - \lambda[O_3] + k_3(t)[NO_2] - k_4[NO][O_3] \quad (25e)$$

$$\partial_t[S(N)GN] = -\partial_x(u \cdot [S(N)GN]) - \lambda[S(N)GN] + 2k_6[NO_2][RP] \quad (25f)$$

where for a specie Z : $[Z](t, x)$ denotes the concentration field ; and for $Z \in \{ROC, NO, NO_2\}$, $E_Z(x) = E_Z^0 \mu(x)$ denotes
 545 the stationary emission field modulated by the smooth ocean/land mask $\mu(x) \in [0, 1]$ shown in Fig. 8(b), and of maximum emission E_Z^0 whose value is given in Table 1 (right column). The ground deposition is represented by terms in λ , with a magnitude of 2% per day. Kinetic parameters and chemical reaction rates are set as follows: since Eq. (25a) and Eq. (25c) depends on the solar radiation, k_1 and k_3 evolve in time to represent the diurnal cycle while they are related by $k_1 = 0.152k_3$ (Fig. 8(c)); the other rates are constant and given in Table 1.

$k_3(t)$	$0.624 \exp\left(-\frac{ (t \equiv 24) - 12 ^3}{100}\right)$	$k_1(t)$	$0.00152k_3(t)$
k_2	12.3	E_{ROC}^0	0.0235
k_4	0.275	E_{NO}^0	0.243
k_5	10.2	$E_{NO_2}^0$	0.027
k_6	0.12	λ	0.02day^{-1}

In k_3 definition, the symbol \equiv corresponds to the modulo operator. Emission rates in ppbCday^{-1} for ROC or ppbday^{-1} for NO_x , and the kinetic rates in $\text{ppb}^{-1} \text{min}^{-1}$, except for k_3 and k_1 in min^{-1} .

Table 1. GRS settings

550 4.2 The PKF for the GRS chemical transport model

In a new numerical experiment, the PKF forecasts will be compared with those of an EnKF (of size 1600). There is no observation assimilation in this simulation.

Given the complexity of the set of equations Eq. (25), and the increased number of species in comparison to the LV-CTM Eq. (13), the equations of the PKF dynamics for the GRS-CTM are not presented in this article, but can be found in additional
 555 material². In this context, the PKF system describes the dynamics of 33 pronostics parameters: 6 mean fields, 6 univariate variances fields, 6 anisotropy fields and 15 cross-covariances fields (corresponding to the number of pairs of chemical species).

²<https://github.com/opannekoucke/pkf-multivariate>

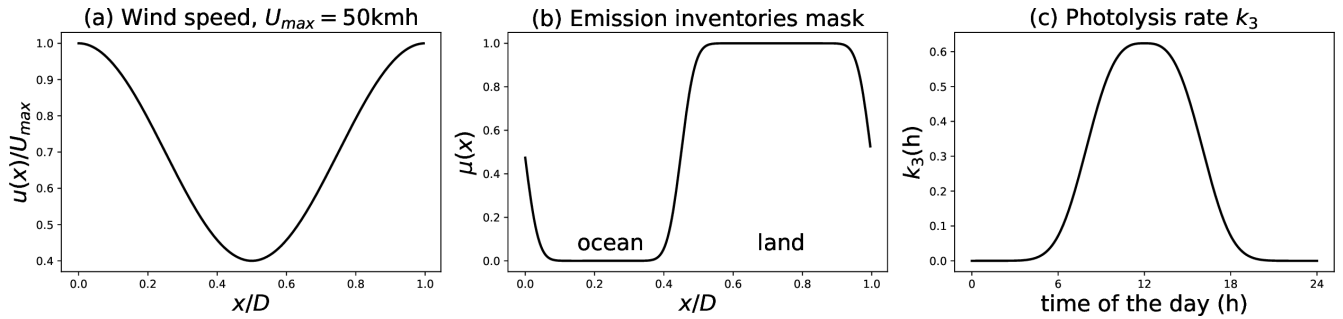


Figure 8. Settings of the GRS-CTM, with the predefined heterogeneous and stationary wind field (panel a) and emission inventories mask (panel b); and with the diurnal cycle of the photolysis rate k_3 (min^{-1}) (panel c), as they are used for the simulation.

In terms of complexity, the PKF dynamics for the GRS-CTM is similar to the simplified LV-CTM: the transport part is the same, while the chemical part presents the same kind of interactions between the chemical species. However, the stationary heterogeneous emissions, not present in LV-CTM, imply a forcing in the dynamics of the mean concentrations in GRS-CTM, but without effect on the uncertainty because the emissions are not stochastic here. Note that uncertainties on emission inventories can be introduced in a PKF formulation *e.g.* as a source term in the variance dynamics, and is related to the specification of boundary conditions in a PKF (Sabathier et al., 2022). Similarly to the LV-CTM, the dynamics of the anisotropy is closed by removing the terms due to the chemistry. Hence, latter, the dynamics of anisotropy in GRS-CTM is only due to the transport.

4.3 Numerical experiment: forecast

For the settings of this numerical experiments, the resolution of the grid has been reduced to $N_x = 241$ grid points, and the time step to $\Delta t = 10^{-4}\text{h}$ to support the stiffness of the GRS equations. Some parameters remain unchanged: RK4 temporal scheme, finite differences to approximate spatial derivatives, choice of the wind field (Fig. 8(a)). The forecast starts at $t_0 = 00\text{h}$ (midnight) and ends at $t = t_0 + 72\text{h}$.

Realistic heterogeneous initial concentration fields are constructed as follows. First, starting from zero concentrations, a chemical equilibrium state is computed from a 4 weeks time integration of a 0D version of Eq. (25) where the transport has been switched off while the concentrations are forced by their respective emissions $E_{(c)}^O$. The resulting concentrations are denoted by $[Z]_{0D}^{4\text{weeks}}$. Then, 1D concentration fields are constructed, defined to be constant and equal for each species to the final value of the 0D integration. The resulting homogeneous concentration fields are then independently perturbed to produce heterogeneous concentration fields, more realistic than the homogeneous concentrations: for any species Z of the 6 chemical species, the resulting 1D perturbed field $[Z]^0(x) = [Z]_{0D}^{4\text{weeks}}(1 + 0.15e(x))$ where $e = \mathbf{P}^{1/2}\zeta$ with \mathbf{P} is a homogeneous Gaussian correlation version of Eq. (7) with variance 1 and constant length-scale $l_h = 12\Delta x$; and ζ is a sample of Gaussian random vector $\mathcal{N}(0, \mathbf{I}_{N_x})$. These perturbed 1D fields of concentrations correspond to the initial condition at $t_0 = 00\text{h}$ of the GRS-CTM simulations.

The initial condition for the PKF is set as follows. The mean state is given by the six 1D fields $[Z]^0(x)$. The multivariate
580 initial uncertainty is set as univariate (no cross-correlation) with a magnitude of $\sigma^0(Z) = 0.15[Z]_{0D}^{4\text{weeks}}$ for each of the six
species, with univariate homogeneous Gaussian correlation of length-scale $15\Delta x$ (60km), the length-scale are identical for all
species.

For the validation, an ensemble of 1600 initial conditions has been populated, consistently from the PKF initial conditions,
by adding univariate perturbations to the GRS-CTM initial condition. For each member k of the ensemble and each field Z
585 that is to perturb, $[Z]_k^0(x) = [Z]^0(x) + 0.15[Z]_{0D}^{4\text{weeks}} e_k(x)$ where $e_k = \mathbf{P}^{1/2} \zeta_k$ with \mathbf{P} is an homogeneous version of Eq. (7)
with variance 1 and constant length-scale $l_h = 15\Delta x$; and ζ is a sample of Gaussian random vector $\mathcal{N}(0, \mathbf{I}_{N_x})$.

Fig. 9 shows the statistics produced by the PKF and the EnKF experiments at two instants: at $t = 00h + 60h$, and at $t =$
 $00h + 66h$. These times corresponds to 12h00 and 18h00 of day 2. Each row features the uncertainty for a specie Z with
respectively: the mean, the standard-deviation, the length-scale and a selection of four cross-correlation functions with NO_2 ,
590 $\rho_Z^{NO_2}$; that is the autocorrelation when Z is NO_2 itself. The choice of NO_2 for the cross-correlation is arbitrary and other
cross-correlations present the same behaviour (not shown).

Regarding the behaviour of the error statistics, the impact of the chemistry appears: the chemical reactions led to non-zero
cross-correlations visible on the right column (except Fig. 9(p) which corresponds to autocorrelations).

The impact of chemistry leads to non-zero cross-correlations between all pairs of species (Fig. 9, right column, except the
595 autocorrelation in Fig. 9(p)) Also, the small-scale spatial variation, that was originally only present on the means, has been
transferred to the standard-deviations fields, except for ROC. The effect of the transport is also present: it produces spatial
heterogeneities on the means (left column), standard-deviations (second column) and length-scales (third column).

Compared to the EnKF, the PKF offers a high quality forecast at a very low computational cost. The means (left column)
are in perfect accordance in both methods. Slight differences can be observed regarding the standard-deviations fields (second
600 column), but as established in Sec. 2.4 (see Appendix A), the EnKF diagnoses are biased by the numerical model error that
is significant when using the low-resolution grid ($N_x = 241$ grid points in this simulation). The same argument applies to
the length-scales (third column), although they may also be govern by some underlying chemical dynamics similar to those
described for Fig. 6(f) in section 3.3.2). Since the PKF formulation considered here is closed by removing the contribution of the
chemistry on the length-scale dynamics (following the simplification discussed in Sec.3.2.2), the length-scale dynamics is the
605 same for all species. Moreover, starting from the same initial constant length-scale field l_h , the length-scale fields predicted by
the PKF are the same for all species. Nevertheless, it does not prevent the PKF from estimating the auto and cross-correlation
functions (right column). The last column presents an important result: the cross-correlation functions estimations by the
proxy are in great accordance with the EnKF. The proxy reproduces the variety of cross-correlation functions such as negative
correlations, small amplitudes, asymmetric structures. Despite differences in length-scales estimations, the proxy shows itself
610 robust and delivers satisfying modeled cross-correlation functions (at a qualitative level). This has been observed for other
cross-correlation functions (not shown here). It demonstrates the capacity of the PKF to forecast the cross-covariance fields.

Note that the specific behavior of the ROC error-variance can be understood from the PKF equations for GRS-CTM (not detailed here but available on the github repository³), where the dynamics of V_{ROC} , which reads as

$$\partial_t V_{ROC} + u \partial_x V_{ROC} = -2V_{ROC} \partial_x u - 2\lambda V_{ROC}, \quad (26)$$

615 is only governed by decay (term in λ) and transport (terms in u), and is not coupled with any means – while a coupling with the means is present for other chemical species. Again, this illustrates the ability of the PKF to explain the physics of uncertainties.

5 Summary and conclusions

This work explored a multivariate formulation of the PKF for atmospheric chemistry needs, when the PKF is formulated from the variance and the anisotropy tensor.

620 While a significant portion of the air quality uncertainty is due to meteorology (*e.g.* the uncertainty of the wind used for the transport), the present work focuses on the situation where the uncertainty in chemical variables is due solely to chemistry as it evolves along a given meteorological situation.

A simplified univariate chemical transport model has been introduced in a 1D periodical domain with a heterogeneous wind field and a conservative dynamics, illustrating the impact of the transport on the error statistics, and in particular the evolution of the variance and of the anisotropy (length-scale) due to the wind heterogeneity. Compared with an estimation from a large ensemble of 6400 forecasts, the PKF has been shown able to reproduce the variance and the anisotropy, and also able to provide a proxy for the correlation functions. The PKF prediction has been obtained at a lower numerical cost compared with the cost of the ensemble. In addition, the PKF has been shown less sensitive to a dispersive model error encountered for this simulation that required computing the ensemble at a high resolution to mitigate the effect of the dispersive term on the ensemble estimation. This simplified model proposed a proxy for multivariate covariance to approximate cross-covariances, which extends the univariate covariance model parameterized from variance and anisotropy, but there resulting multivariate covariance is symmetric with no guarantee of positiveness.

630 Then a simplified multivariate chemical transport model has been introduced to tackle multivariate error statistics. Based on Lotka-Volterra (LV) dynamics, this testbed reproduces non-linear coupling between chemical species as well as the transport due to the wind, as it can be observed in real chemical transport model. Then a multivariate PKF formulation has been proposed, which made appear a closure issue related to the chemical part, but not to the transport, and concerns the dynamics of the anisotropy. A detailed analysis of the effect of the chemistry on the dynamics of the anisotropy led to an analytical solution of the multivariate evolution of the uncertainty in a 1D harmonic oscillator, which helps to understand the transfer of uncertainty from one species to another.

640 The PKF has permitted the understanding of the uncertainties dynamics: it offered equations that described the time evolutions of variances, cross-covariances and anisotropies. The impact of the advection and of the chemistry have been clearly identified in the dynamics of the error statistics, allowing for a better comprehension of the overall problem. Since the relative

³see https://github.com/opannekoucke/pkf-multivariate/blob/master/notebooks/annexe_notebooks/computing_grs_dynamics_with_sympkf.ipynb

contribution of the transport was larger than the one of the chemistry in the trend of the anisotropy, a closed form has been considered by removing the terms related to the chemistry in the dynamics of the anisotropy.

645 Despite of this approximation, a validation test-bed using an ensemble method shown the that PKF dynamics is able to predict the uncertainty dynamics for two chemical schemes based on LV. Moreover, a multivariate formulation of the PKF analysis step has been introduced, given by Algorithm 1, and several assimilation cycles have been conducted for the LV chemical scheme, showing the a multivariate PKF assimilation is possible, which is promising.

A final multivariate example, focused on the forecast step, has been introduced to evaluate the potential of the multivariate
650 PKF formulation to a larger system. In this case, the chemical scheme (GRS) describe the interaction of six species. Again, this example has shown the ability of the PKF to reproduce the EnKF error statistics.

To go further, it will be interesting to see if the advection terms remain dominant under different conditions like weaker wind or accelerated chemistry from an ensemble of forecasts of operational CTMs, where isotropic and homogeneous correlations are often considered in variational data assimilation.

655 In addition, since we have focused on the uncertainty due to chemistry, it would be interesting to address the part of the uncertainty due to meteorology. For a CTM like MOCAGE, this could be done by considering an ensemble of weather forecasts with each member used as a forcing for a single CTM forecast. However, this solution would lead to multiple CTM forecasts, which would be expensive. Therefore, from the perspective of using a PKF (applied to a CTM), a less expensive solution would be to consider a single PKF forecast where the wind is uncertain (stochastic advection wind), with the wind uncertainty
660 characterized by the variance and anisotropy tensor estimated from the weather forecast ensemble. The challenge will be to find an appropriate closure for the unknown terms in the dynamics, including the cross-correlation between the wind error and chemical species, with the help of this contribution on multivariate statistics.

This work is a milestone in the development of a multivariate assimilation based on the PKF and applied to air quality, and is an important step in extending the univariate PKF implementation to complex operational CTMs like the operational transport
665 model MOCAGE at Meteo-France. The work also highlight a drawback of the PKF: the cost of the current multivariate PKF formulation scales as the square of number of chemical species which appears as a limitation, at least if all the chemical species are considered in the multivariate uncertainty prediction. Hence, it would be interesting to test a PKF formulation on a reduced chemical scheme of interest for the data assimilation.

Moreover, while this contributions focused on air quality, it contributes to improve our understanding of multivariate statis-
670 tics *e.g.* with the analytical solution of the 1D harmonic oscillator. It would be interesting to extend this multivariate PKF formulation to other geophysical applications *e.g.* the numerical weather prediction ; with a particular attention on the extension of the multivariate cross-covariance proxy to the 2D or 3D domains. Compared with air quality where the chemical reactions are point-wise, geophysical equations make appear local interactions that have to be studied in view of the PKF approach *e.g.* the geostrophic balance in the barotropic model.

675 *Code and data availability.* The code developed and used to generate the experiments is available under <https://github.com/opannekoucke/pkf-multivariate>

Appendix A: Limits of the numerical validation of the PKF in presence of model error

The exploration of the uncertainty dynamics from numerical experiments, as made here to validate the PKF from an ensemble method, faces some limits. Figure 2 has shown a gap between the PKF and EnKF regarding the forecast of the error statistics
 680 (standard deviation Fig 2(b) and length-scales Fig 2(c)). We now justify this observation, relating it to a model error.

As the problem is discretized for numerical simulations, the actual equation that is simulated is not exactly Eq. (9a), but rather an implicit modified equation induced by the use of finite differences for the spatial and the temporal discretisation. Focusing on the spatial discretization, the modified equation writes

$$\partial_t \mathcal{X} = -u \partial_x \mathcal{X} - \mathcal{X} \partial_x u - \frac{\Delta x^2}{6} u \partial_x^3 \mathcal{X} - \frac{\Delta x^2}{6} \mathcal{X} \partial_x^3 u + \mathcal{O}(\Delta x^3), \quad (\text{A1})$$

685 which shows additional dispersive terms not present in the initial dynamics (Eq. 9a). Note that Eq. (A1) is not the full modified equation of the discretized model, in particular it does not represent the effect of the RK4 time scheme, but the error associated to fourth-order time scheme should be negligible compared with the spatial numerical error (second-order). Hence, Eq. (A1) should be close to the true modified equation, and the presence of additional processes may explain the significant differences observed in Fig. 2-(b) and (c): the dispersive term $-\frac{\Delta x^2}{6} u \partial_x^3 \mathcal{X}$ contributes to reduce the speed of the transport to a value lower
 690 than u , while the term $-\frac{\Delta x^2}{6} \mathcal{X} \partial_x^3 u$ implies a local exponential growing (damping) of $\mathcal{X}(t, x)$ where $\partial_x^3 u$ is negative (positive). This exponential evolution only contributes to the magnitude of the forecast-error *i.e.* it modifies the variance field but it has no influence on the length-scale (Pannekoucke et al., 2018). At the opposite, the dispersive term influences both the variance and the length-scale as it can be observed in Fig. 2-(c): the EnKF curves appear slightly late behind the PKF ones (the wind transports the curves toward the right), presenting a negative shift in the amplitude.

695 This can be understood as follows. Since Eq. (A1) is linear, it is the dynamics of the mean and of the errors in the numerical experiment. But the typical scale of the mean and of the error are different: in this simulation, the spatial scale of the mean state is large, of the order of D , while the spatial scale of the errors is of order $l_h \approx D/16$, where $16 \approx 241/15$; this implies that the magnitude of the negative phase shift due to the dispersive term is larger for the error than for the mean (see *e.g.* KdV Eq. (1.19) in Whitham (1999), p.9).

700 This justifies why the dispersion does not affect the prediction of the mean state – the estimation for the means coinciding for the two methods on Fig. 2-(a) –, while it acts on the EnKF predictions of the variance and of the length-scale, related to the error dynamics. In this simulation, the PKF Eq. (10) is not influenced by the dispersion because the spatial scale of the variance and of the length-scale fields is large (order of D). This points out the sensitivity of the EnKF to numerical model error.

Since the magnitude of the dispersive term scales as $\mathcal{O}(\Delta x^2)$, a simulation at high resolution could damp this term and
 705 would lead to attributing the gap observed in Fig. 2 to the model error.

This is demonstrated by comparing the PKF statistics to a high resolution forecast of the EnKF with a grid of three times the original resolution *i.e.* $N_x = 3 \times 241 = 723$ grid points. To be consistent with the initial low resolution experiment, the initial

length-scale of the high resolution is set to $l_h^0 = 3 \times 15\Delta x = 45\Delta x \simeq 62.2\text{km}$. The time step has been adapted in consequence to match the CFL condition. The results of this new simulation, in Fig. A1, show that predicting the ensemble at high resolution leads to the same variance (Fig. A1(b)) and length-scale (Fig. A1(c)) fields as the ones predicted by the PKF, while the latter is computed at low resolution. A PKF at high resolution has been computed (not shown here) and has been found equivalent to the PKF computed at low resolution, with a relative error at the end of the forecast window lower than 0.2% for the mean, 0.3% for the standard-deviation, and 0.05% for the length-scale ; where the relative error of fields has been computed as $\|PKF_{LR} - PKF_{HR}\|/\|PKF_{HR}\|$, with $\|\cdot\|$ the L2 norm. This demonstrates the quality of the forecasted error statistics for the PKF, even at a low resolution. Figure B1 also shows the correlation functions computed from the high resolution EnKF forecast. The correlation functions represented are in better accordance with the PKF modelled correlation functions than for the low resolution ensemble forecast, see *e.g.* Fig. B1(d) to Fig. B1(f). This shows that the PKF is little subject to numerical model error as the error statistics forecasts directly results from their time-integration. Compared to previous studies that focused only on the comparison of variance and anisotropy error statistics, here we have shown the ability to reproduce complex heterogeneous correlation functions using the PKF formulation in 1D domain.

Appendix B: Validation of correlation functions in univariate situations

Figure B1 compares the correlation functions at position $x_l = 0.5$, estimated from the ensemble for the EnKF and modeled from the predicted parameters for the PKF when using Eq. (7), at different times. At a qualitative level, the PKF is able to approximate the correlation functions, the latter being only known to within a sampling noise because of the ensemble estimation which is assumed low due to the ensemble size. In particular, the PKF is able to reproduce the large (the small) spread of the symmetric correlations present in Fig. B1(a) (Fig. B1(b)). But the PKF is also able to represent the anisotropy of the correlations as the one shown *e.g.* in Fig. B1(e) where the correlation function at that time appears broader on its right part (corresponding to x larger than x_l) than on its left part (corresponding to x smaller than x_l).

Appendix C: Lotka-Volterra chemical model

We consider four chemical species A, B, X and Y governed by the chemical reactions:



The kinetic of the reaction, deduced from the mass action law for reaction rate writes:

$$735 \quad \frac{d[A]}{dt} = k_1[X][A] - k_2[A][B] \quad (\text{C4a})$$

$$\frac{d[B]}{dt} = k_2[A][B] - k_3[B] \quad (\text{C4b})$$

where $[\cdot]$ denotes the concentration. When the concentrations of X and Y are constant, the system simplifies as:

$$\frac{d[A]}{dt} = k_1[A] - k_2[A][B] \quad (\text{C5a})$$

$$\frac{d[B]}{dt} = k_2[A][B] - k_3[B] \quad (\text{C5b})$$

740 which is a Lotka-Volterra system.

Appendix D: Contribution of the chemistry to the uncertainty dynamics in the LV-CTM

This section contributes to evaluate the impact of chemistry on the dynamics of uncertainty with respect to the effect due to advection, leading to a closure for the PKF applied to the multivariate LV-CTM.

D1 Impact of the chemistry alone on the dynamics of the anisotropies for homogeneous statistical initial conditions

745 Regarding the dynamics of the anisotropy fields presented in the prognostic equations (Eq. (20f)-Eq. (20g)), the part due to transport in $T_{adv-(\cdot)}^{(\cdot)}$ is already well understood, as it comes down to the univariate case presented in Sec. 2.4. However, the role of the chemistry in $T_{chem-(\cdot)}^{(\cdot)}$ is unclear at this time. The transport process is removed to focus on the dynamics of the anisotropy due to the chemistry.

In the PKF dynamics in Eq. (20), when there is no transport and when the variance fields are homogeneous at the initial
750 condition, the homogeneity is preserved during the time evolution. Hence, the spatial derivatives of the variance and of the cross-variance fields are null, which leads to simplify the dynamics of the anisotropy (Eq. (20f)-Eq. (20g)) as

$$\partial_t s_A = \frac{2k_2 A s_A}{\sigma_A} \left(\sigma_B s_A \overline{\partial_x \tilde{\varepsilon}_A \partial_x \tilde{\varepsilon}_B} - \frac{V_{AB}}{\sigma_A} \right), \quad (\text{D1a})$$

$$\partial_t s_B = \frac{2k_2 B s_B}{\sigma_B} \left(\frac{V_{AB}}{\sigma_B} - \sigma_A s_B \overline{\partial_x \tilde{\varepsilon}_A \partial_x \tilde{\varepsilon}_B} \right). \quad (\text{D1b})$$

To focus on the contribution of the chemistry on the dynamics of the anisotropies, an ensemble of $Ne = 1600$ high resolution
755 forecasts is performed ($N_x = 723$), with only the chemistry part. Hence, the transport terms are set to zero in Eq. (13). Two numerical experiments are conducted: first, the initial length-scales are equal for both species with $l_A^0 = l_B^0 = 45\Delta x \simeq 62\text{km}$ (results are shown in Fig. D1), then different with $l_A^0 = 45\Delta x$ and $l_B^0 = 66\Delta x \simeq 91\text{km}$ (results in Fig. D2). The initial conditions for the concentrations, and the multivariate statistics are chosen homogeneous over the domain in both cases. Therefore,

only the time series of the spatial average are shown for the variance, the cross-correlation, the length-scale and the open term
760 $\overline{\partial_x \tilde{\varepsilon}_A \partial_x \tilde{\varepsilon}_B}$ which is estimated from the ensemble by

$$\partial_x \widehat{\tilde{\varepsilon}_A \partial_x \tilde{\varepsilon}_B} = \frac{1}{N_e} \sum_{k=1}^{N_e} \partial_x \tilde{\varepsilon}_{A,k} \partial_x \tilde{\varepsilon}_{B,k}, \quad (\text{D2})$$

where $\tilde{\varepsilon}_{A,k} = \varepsilon_{A,k} / \widehat{V}_A$ and $\tilde{\varepsilon}_{B,k} = \varepsilon_{B,k} / \widehat{V}_B$.

In the first experiment, Fig. D1, the magnitude of the error, given by the standard deviations Fig. D1(a), oscillates with a
phase shift where the magnitude of the error in A advances the one of B . The cross-correlation Fig. D1(c) and the unclosed
765 term $\overline{\partial_x \tilde{\varepsilon}_A \partial_x \tilde{\varepsilon}_B}$ Fig. D1(g) oscillate in a similar way. In this experiment, where the initial length-scales are identical for A and
 B , there is no time evolution of the length-scales, except the fluctuations that are due to the sampling noise (see Fig. D1(e)).
The second experiment, Fig. D2, shows roughly the same picture, except that this time, with initial length-scales of different
values, oscillations are appearing Fig. D2(e). Since, *a priori*, it is not easy to track the reason for the change of behaviour
observed on the length-scale dynamics, an analytical investigation of the harmonic oscillator (HO)

$$770 \quad \partial_t A(t, \mathbf{x}) = -k B(t, \mathbf{x}), \quad (\text{D3a})$$

$$\partial_t B(t, \mathbf{x}) = k A(t, \mathbf{x}), \quad (\text{D3b})$$

is introduced, with $k = k_2$. The comparison with HO is relevant since it is an example of analytical multivariate dynamics and
also because it mimics the periodic oscillations of LV, explaining the numerical results. For HO, it is possible to calculate the
time evolution of the statistics analytically (see Appendix E for details), which writes as

$$775 \quad V_A(t) = \cos(kt)^2 V_A^0 + \sin(kt)^2 V_B^0, \quad (\text{D4a})$$

$$V_B(t) = \sin(kt)^2 V_A^0 + \cos(kt)^2 V_B^0, \quad (\text{D4b})$$

$$V_{AB}(t) = \cos(kt) \sin(kt) (V_A^0 - V_B^0), \quad (\text{D4c})$$

$$s_A(t) = V_A(t) \left[\cos(kt)^2 \frac{V_A^0}{s_A^0} + \sin(kt)^2 \frac{V_B^0}{s_B^0} \right]^{-1}, \quad (\text{D4d})$$

$$s_B(t) = V_B(t) \left[\sin(kt)^2 \frac{V_A^0}{s_A^0} + \cos(kt)^2 \frac{V_B^0}{s_B^0} \right]^{-1}, \quad (\text{D4e})$$

$$780 \quad \overline{\partial_x \tilde{\varepsilon}_A \partial_x \tilde{\varepsilon}_B}(t) = \frac{\cos(kt) \sin(kt)}{\sigma_A(t) \sigma_B(t)} \left[\frac{V_A^0}{s_A^0} - \frac{V_B^0}{s_B^0} \right]. \quad (\text{D4f})$$

Numerical results computed for the HO are represented in Fig. D1 and Fig. D2, and show some of the behaviour encountered
for the nonlinear LV equations. For instance, the oscillations of the variance are visible. Moreover, the length-scales oscillate
depending on the initial condition: when the initial length-scales are equal, there is no oscillation (see Fig. D1-(f)) that appear
from the analytical computation of s_A and s_B ; in contrast, for different values of the initial length-scales, oscillations appear
785 (see Fig. D2-(f)). These different behaviours of the anisotropy based on the initial settings of the length-scales are explained
by the analytical solutions of the error statistics for the harmonic oscillator. For instance, when plugging the identical initial
condition for the length-scales $s_A^0 = s_B^0$ and the analytical solution of $V_A(t)$ (Eq. D4a) into the r.h.s. of Eq. (D4d), it simplifies

to $s_A(t) = s_A^0$. The same result applies for $s_B(t)$. This simplification no longer holds when $C \neq s_B^0$, leading to non-constant length-scales which is effectively observed.

790 Note that for equal initial length-scales, the anisotropy appears stationary (see Fig. D1(e)), which suggests a closure for the open term $\overline{\partial_x \tilde{\varepsilon}_A \partial_x \tilde{\varepsilon}_B}$: since the anisotropy is equal and constant, $s_A(t) = s_B(t) = \frac{s_A(t) + s_B(t)}{2} = s_A^0 = s_B^0 = \frac{s_A^0 + s_B^0}{2}$, then from the stationarity of the anisotropy, $\partial_t s_A = \partial_t s_B = 0$, the right-hand side of Eqs. (D1) leads to the expression

$$\overline{\partial_x \tilde{\varepsilon}_A \partial_x \tilde{\varepsilon}_B} = \frac{V_{AB}(x)}{\sigma_A(x)\sigma_B(x)} \frac{2}{s_A(x) + s_B(x)}. \quad (\text{D5})$$

This closure indicates that the term $\overline{\partial_x \tilde{\varepsilon}_A \partial_x \tilde{\varepsilon}_B}$ is proportional to the cross-correlation in this particular case. This is confirmed in Fig. D1, where $\overline{\partial_x \tilde{\varepsilon}_A \partial_x \tilde{\varepsilon}_B}$ Fig. D1(g) appears to evolve as the cross-correlation Fig. D1(c). For this specific case, Eq. (D5) also applies for the error statistics of the harmonic oscillator: using $s_A^0 = s_B^0$ and the time evolution of the cross-covariance V_{AB} (Eq. D4c) allows to solve for the open term in Eq. (D4f), obtaining the same expression as in Eq. (D5).

The time evolution of the HO error statistics makes appear an alternate transfer of the error statistics between the two components A and B , which qualitatively reproduces the evolution observed in the LV dynamics. The transfer of uncertainty from one component to the other is provided by the cross-covariance V_{AB} when the error variance is different for each of the two species.

D2 Detailed contribution of each processes in the dynamics of the anisotropy

The following section aims at identifying the dominant terms, or processes in the dynamics of the anisotropy, Eq. (20f) and Eq. (20g).

805 Two different evaluations are performed. The first one evaluates the relative contribution $W_{Z,j}$ of the term $T_{Z,j}$ with respect to all other terms in the dynamics of the anisotropy of Z , which reads as

$$W_{Z,j}(t) = \frac{\|T_{Z,j}(t)\|_1}{\sum_k \|T_{Z,k}(t)\|_1}, \quad (\text{D6})$$

where $\|v\|_1 = \frac{1}{N_x} \sum_{j=1, \dots, N_x} |v_j|$ is the L^1 norm on the discretized domain $[0, D]$. The second one evaluates the relative contribution of each physical processes in the dynamics of the anisotropy *e.g.* the relative contribution of the advection in the dynamics of the anisotropy of Z , $W_{Z,adv}$, reads as

$$W_{Z,adv}(t) = \frac{\|\sum_{k=1}^2 T_{Z,adv-k}(t)\|_1}{\|\sum_{k=1}^2 T_{Z,adv-k}(t)\|_1 + \|\sum_{k=1}^5 T_{Z,chem-k}(t)\|_1}, \quad (\text{D7})$$

from which the relative contribution of the chemistry writes $W_{Z,chem}(t) = 1 - W_{Z,adv}(t)$. Note that the normalization is different between Eq. (D6) and Eq. (D7).

The computation of these relative contributions will rely on ensemble of forecasts. They will be used to diagnose *a posteriori* the PKF parameters $(A, B, V_A, V_B, V_{AB}, s_A, s_B)$ as well as the three open terms $(\overline{\partial_x \tilde{\varepsilon}_A \partial_x \tilde{\varepsilon}_B}, \overline{\tilde{\varepsilon}_A \partial_x \tilde{\varepsilon}_B}, \overline{\tilde{\varepsilon}_B \partial_x \tilde{\varepsilon}_A})$ to then reconstruct all the terms in the anisotropy dynamics (Eq. (20f)-Eq. (20g)).

The quantifications of the relative contribution by term and by process will be performed for equal and different initial length-scales for A and B , as they lead to different dynamics for the anisotropy. Thus, two ensembles are forecasted, with initial length-scales set to $l_A^0 = l_B^0 = 45\Delta x$ in the first, and $l_A^0 = 45\Delta x$ and $l_B^0 = 66\Delta x$ in the second. A high resolution grid is considered ($N_x = 723$) to reduce numerical model error; the time step has been adapted in consequence to match the CFL. The other settings as well as the numerical configuration for this experiment are unchanged from previous ensemble forecast performed in Sec. 3.1.2.

The results of the relative contributions presented in Fig. D3 (Fig. D4) for the equal (different) length-scale configuration are now discussed. Regarding the relative contribution by process experiment, the comparison between panels Fig. D3(c) (Fig. D3(d)) and Fig. D4(c) (Fig. D4(d)) indicates that when the initial length-scales are different, $l_A^0 \neq l_B^0$, the chemistry has a more significant role (W_{chem} is about 21%) compared when the length-scales are equal (W_{chem} is about 10%) in the dynamics of the anisotropies. That difference was expected following the results obtained in Appendix D1. Now focusing on the relative contribution by term on panels (a) and (b) of Fig. D3 and Fig. D4, it is noticeable that only the two terms, W_{chem-1}^Z and W_{chem-2}^Z , have a significant role in the dynamics. The rest of the chemistry-related terms magnitudes are negligible. For equal initial length-scales, as the chemistry-related part of the anisotropy dynamics can be neglected compared to the advection part (Fig. D3c,d), and as this part is mainly driven by W_{chem-1}^Z and W_{chem-2}^Z (Fig. D3a,b), this means an approximate compensation of the two terms. Eventually, this approximation simplifies to Eq. (D5), which is in accordance with the previous results of Appendix D1. However, this approximation becomes invalid in the heterogeneous case: the terms W_{chem-1}^Z and W_{chem-2}^Z no longer compensate each other as the gap between their corresponding curves increases in panels Fig. D4(c) and Fig. D4(d). In some other numerical trials (not shown here), this approximation was used regardless of the length-scales initial configuration, and the remaining open terms were set to zero. These trials produced incoherent forecasts for the anisotropy, pointing out the incapacity of the approximation to capture the true complexity of the unknown terms. Subsequently, this approximation is no longer retained.

Appendix E: Dynamics of the error statistics for the Harmonic Oscillator

The harmonic oscillator equations writes:

$$\partial_t A = -k B, \tag{E1a}$$

$$\partial_t B = k A, \tag{E1b}$$

with $A = A(t, x)$ and $B = B(t, x)$ being functions of time and 1D space. As this problem is linear, the dynamic is identical for the errors,

$$\partial_t \varepsilon_A = -k \varepsilon_B, \tag{E2a}$$

$$\partial_t \varepsilon_B = k \varepsilon_A. \tag{E2b}$$

Their analytical solution is given by:

$$\varepsilon_A(t, x) = \cos(kt)\varepsilon_A(0, x) - \sin(kt)\varepsilon_B(0, x), \quad (\text{E3a})$$

$$\varepsilon_B(t, x) = \sin(kt)\varepsilon_A(0, x) + \cos(kt)\varepsilon_B(0, x). \quad (\text{E3b})$$

850 At the initial time, we consider the case where the error are uncorrelated $V_{AB}^0 = \mathbb{E}[\varepsilon_A^0 \varepsilon_B^0] = 0$ and where the variance and length-scale fields are homogeneous, *i.e.* $\partial_x V_A^0 = \partial_x V_B^0 = \partial_x g_A^0 = \partial_x g_B^0 = 0$; where the upper-script \cdot^0 is a shorthand for denoting the fields a initial time.

From the analytical solution for the errors Eq. (E3), we deduce solutions for the error statistics.

$$V_A(t, x) = \mathbb{E} \left[(\varepsilon_A(t, x))^2 \right] \quad (\text{E4a})$$

$$855 \quad = \cos^2(kt)\mathbb{E}[\varepsilon_A^2](0, x) - 2\cos(kt)\sin(kt)\mathbb{E}[\varepsilon_A \varepsilon_B](0, x) + \sin^2(kt)\mathbb{E}[\varepsilon_B^2](0, x) \quad (\text{E4b})$$

$$= \cos^2(kt)V_A^0 - 2\cos(kt)\sin(kt)\underbrace{V_{AB}^0}_{=0} + \sin^2(kt)V_B^0 \quad (\text{E4c})$$

$$= \cos^2(kt)V_A^0 + \sin^2(kt)V_B^0 \quad (\text{E4d})$$

Following the same process, we deduce that $V_B(t, x) = \sin^2(kt)V_A^0 + \cos^2(kt)V_B^0$ and $V_{AB}(t, x) = \cos(kt)\sin(kt)(V_A^0 - V_B^0)$. We can now determine the dynamics of the metric tensor:

$$860 \quad g_A(t, x) = \mathbb{E} \left[\left(\partial_x \left(\frac{\varepsilon_A}{\sqrt{V_A}} \right) \right)^2 \right] (t, x) \quad (\text{E5a})$$

$$= \mathbb{E} \left[\left(\frac{\partial_x \varepsilon_A}{\sqrt{V_A}} - \frac{\varepsilon_A \partial_x V_A}{2V_A^{3/2}} \right)^2 \right] (t, x) \quad (\text{E5b})$$

As we consider homogeneous fields, we have that $\partial_x V_A = 0$, simplifying the expression to

$$g_A(t, x) = \frac{1}{V_A} \mathbb{E} [(\partial_x \varepsilon_A)^2] (t, x) \quad (\text{E6a})$$

$$= \frac{1}{V_A(t, x)} \mathbb{E} \left[\cos^2(kt) (\partial_x \varepsilon_A^0)^2 - 2\cos(kt)\sin(kt)\partial_x \varepsilon_A^0 \partial_x \varepsilon_B^0 + \sin^2(kt) (\partial_x \varepsilon_B^0)^2 \right] (x) \quad (\text{E6b})$$

865 Then, at $t = 0$, $\mathbb{E}[(\partial_x \varepsilon_A^0)^2]$ simplifies to $V_A^0 g_A^0$ and $\mathbb{E}[(\partial_x \varepsilon_B^0)^2] = V_B^0 g_B^0$. The independence of ε_A^0 and ε_B^0 also implies $\mathbb{E}[\partial_x \varepsilon_A^0 \partial_x \varepsilon_B^0] = 0$. Finally, we obtain that:

$$g_A(t, x) = \frac{1}{V_A(t, x)} [\cos^2(kt)V_A^0 g_A^0 + \sin^2(kt)V_B^0 g_B^0]. \quad (\text{E7})$$

We can also deduce an analytical solution for the term $\mathbb{E}[\partial_x \tilde{\varepsilon}_A \partial_x \tilde{\varepsilon}_B]$ which reads, under assumption of homogeneity, as:

$$\mathbb{E}[\partial_x \tilde{\varepsilon}_A \partial_x \tilde{\varepsilon}_B](t, x) = \mathbb{E} \left[\left(\partial_x \frac{\varepsilon_A}{\sqrt{V_A}} \right) \partial_x \left(\frac{\varepsilon_B}{\sqrt{V_B}} \right) \right](t, x) \quad (\text{E8a})$$

870

$$= \frac{1}{(\sqrt{V_A} \sqrt{V_B})(t, x)} \mathbb{E}[\partial_x \varepsilon_A \partial_x \varepsilon_B](t, x) \quad (\text{E8b})$$

$$= \frac{1}{\sigma_A(t) \sigma_B(t)} \mathbb{E} \left[\cos(kt) \sin(kt) \left((\partial_x \varepsilon_A^0)^2 - (\partial_x \varepsilon_B^0)^2 \right) + \partial_x \varepsilon_A^0 \partial_x \varepsilon_B^0 (\cos^2(kt) - \sin^2(kt)) \right](t, x) \quad (\text{E8c})$$

$$= \frac{1}{\sigma_A(t) \sigma_B(t)} \left(\cos(kt) \sin(kt) \left(\underbrace{\mathbb{E}[(\partial_x \varepsilon_A^0)^2]}_{V_A^0 g_B^0} - \underbrace{\mathbb{E}[(\partial_x \varepsilon_B^0)^2]}_{V_B^0 g_B^0} \right) + \underbrace{\mathbb{E}[\partial_x \varepsilon_A^0 \partial_x \varepsilon_B^0]}_{=0} (\cos^2(kt) - \sin^2(kt)) \right)(t, x) \quad (\text{E8d})$$

$$= \frac{\cos(kt) \sin(kt)}{(\sigma_A \sigma_B)(t, \mathbf{x})} (V_A^0 g_B^0 - V_B^0 g_B^0). \quad (\text{E8e})$$

Note that we could have derived analytical solutions in the case of heterogeneous initial fields, but for the sake of simplicity we chose to consider only the homogeneous case. However, obtaining analytical solution when the initial error fields are correlated seems more difficult.

Appendix F: Cross-covariance analysis formula demonstration

By introducing the true state and the error fields $\mathcal{X}^a = \mathcal{X}^t + \varepsilon^a$, $\mathcal{X}^f = \mathcal{X}^t + \varepsilon^f$ and $\mathcal{Y}^o(\mathbf{x}_l) = \mathcal{X}^t(\mathbf{x}_l) + \varepsilon^o(\mathbf{x}_l)$, the analysis equation (8a) becomes:

$$\varepsilon^a(\mathbf{x}) = \varepsilon^f(\mathbf{x}) + \sigma^f(\mathbf{x}) \rho_{\mathbf{x}_l}^f(\mathbf{x}) \frac{\sigma^f(\mathbf{x}_l)}{V^f(\mathbf{x}_l) + V^o(\mathbf{x}_l)} (\varepsilon^o(\mathbf{x}_l) - \varepsilon^f(\mathbf{x}_l)) \quad (\text{F1})$$

which can be adapted to the multivariate case:

$$\varepsilon_{Z_1}^a(\mathbf{x}) = \varepsilon_{Z_1}^f(\mathbf{x}) + \sigma_{Z_1}^f(\mathbf{x}) \rho_{Z_1 Z_l, l}^f(\mathbf{x}) \frac{\sigma_{Z_l}^f(\mathbf{x}_l)}{V_{Z_l}^f(\mathbf{x}_l) + V_{Z_l}^o(\mathbf{x}_l)} (\varepsilon_{Z_l}^o(\mathbf{x}_l) - \varepsilon_{Z_l}^f(\mathbf{x}_l)) \quad (\text{F2})$$

where Z_l is the chemical species that is observed, Z_1 can be any chemical species, and $\rho_{Z_l Z_l, l}^f(\mathbf{x}) = \mathbb{E}[\varepsilon_{Z_l}^f(\mathbf{x}_l) \varepsilon_{Z_l}^f(\mathbf{x})] / (\sigma_{Z_l}^f(\mathbf{x}_l) \sigma_{Z_l}^f(\mathbf{x}))$ is the forecast *cross*-correlation function between Z_l and Z_1 at location \mathbf{x}_l . Writing the same equation for another chemical Z_2

885

$$\varepsilon_{Z_2}^a(\mathbf{x}) = \varepsilon_{Z_2}^f(\mathbf{x}) + \sigma_{Z_2}^f(\mathbf{x}) \rho_{Z_2 Z_l, l}^f(\mathbf{x}) \frac{\sigma_{Z_l}^f(\mathbf{x}_l)}{V_{Z_l}^f(\mathbf{x}_l) + V_{Z_l}^o(\mathbf{x}_l)} (\varepsilon_{Z_l}^o(\mathbf{x}_l) - \varepsilon_{Z_l}^f(\mathbf{x}_l)) \quad (\text{F3})$$

and using the definition of the analysis error covariance field $V_{Z_1, Z_2}^a(\mathbf{x}) = \mathbb{E} [\varepsilon_{Z_1}^a(\mathbf{x}) \varepsilon_{Z_2}^a(\mathbf{x})]$ leads to

$$\begin{aligned}
V_{Z_1, Z_2}^a(\mathbf{x}) &= \underbrace{\mathbb{E} [\varepsilon_{Z_1}^f(\mathbf{x}) \varepsilon_{Z_2}^f(\mathbf{x})]}_{=V_{Z_1, Z_2}^f(\mathbf{x})} + \frac{\sigma_{Z_l}^f(\mathbf{x}_l)}{V_{Z_l}^f(\mathbf{x}_l) + V_{Z_l}^o(\mathbf{x}_l)} \mathbb{E} \left[\left(\sigma_{Z_2}^f(\mathbf{x}) \rho_{Z_2, Z_l, l}^f(\mathbf{x}) \varepsilon_{Z_1}^f(\mathbf{x}) + \sigma_{Z_1}^f(\mathbf{x}) \rho_{Z_1, Z_l, l}^f(\mathbf{x}) \varepsilon_{Z_2}^f(\mathbf{x}) \right) \left(\varepsilon_{Z_l}^o(\mathbf{x}_l) - \varepsilon_{Z_l}^f(\mathbf{x}_l) \right) \right] \\
&+ \frac{\left(\sigma_{Z_l}^f(\mathbf{x}_l) \right)^2}{\left(V_{Z_l}^f(\mathbf{x}_l) + V_{Z_l}^o(\mathbf{x}_l) \right)^2} \sigma_{Z_1}^f(\mathbf{x}) \rho_{Z_1, Z_l, l}^f(\mathbf{x}) \sigma_{Z_2}^f(\mathbf{x}) \rho_{Z_2, Z_l, l}^f(\mathbf{x}) \mathbb{E} \left[\left(\varepsilon_{Z_l}^o(\mathbf{x}_l) - \varepsilon_{Z_l}^f(\mathbf{x}_l) \right)^2 \right]
\end{aligned} \tag{F4a}$$

890 Then, using the definition of the cross-correlation function $\mathbb{E} [\varepsilon_{Z_l}^f(\mathbf{x}_l) \varepsilon_{Z_1}^f(\mathbf{x})] = \sigma_{Z_l}^f(\mathbf{x}_l) \sigma_{Z_1}^f(\mathbf{x}) \rho_{Z_1, Z_l, l}^f(\mathbf{x})$, the independence between the forecast and observation errors $\mathbb{E} [\varepsilon_{Z_l}^f(\mathbf{x}_l) \varepsilon_{Z_1}^o(\mathbf{x}_l)] = 0$, and the definitions of the observation error variance $V_{Z_l}^o(\mathbf{x}_l) = \mathbb{E} \left[\left(\varepsilon_{Z_l}^o(\mathbf{x}_l) \right)^2 \right]$ and forecast error $V_{Z_l}^f(\mathbf{x}_l) = \mathbb{E} \left[\left(\varepsilon_{Z_l}^f(\mathbf{x}_l) \right)^2 \right]$, we obtain that:

$$\begin{aligned}
V_{Z_1, Z_2}^a(\mathbf{x}) &= V_{Z_1, Z_2}^f(\mathbf{x}) - \frac{\sigma_{Z_l}^f(\mathbf{x}_l)}{V_{Z_l}^f(\mathbf{x}_l) + V_{Z_l}^o(\mathbf{x}_l)} \left(\sigma_{Z_2}^f(\mathbf{x}) \rho_{Z_2, Z_l, l}^f(\mathbf{x}) \sigma_{Z_l}^f(\mathbf{x}_l) \sigma_{Z_1}^f(\mathbf{x}) \rho_{Z_1, Z_l, l}^f(\mathbf{x}) + \sigma_{Z_1}^f(\mathbf{x}) \rho_{Z_1, Z_l, l}^f(\mathbf{x}) \sigma_{Z_l}^f(\mathbf{x}_l) \sigma_{Z_2}^f(\mathbf{x}) \rho_{Z_2, Z_l, l}^f(\mathbf{x}) \right) \\
&+ \frac{V_{Z_l}^f(\mathbf{x}_l)}{\left(V_{Z_l}^f(\mathbf{x}_l) + V_{Z_l}^o(\mathbf{x}_l) \right)^2} \sigma_{Z_1}^f(\mathbf{x}) \rho_{Z_1, Z_l, l}^f(\mathbf{x}) \sigma_{Z_2}^f(\mathbf{x}) \rho_{Z_2, Z_l, l}^f(\mathbf{x}) \left(V_{Z_l}^o(\mathbf{x}_l) + V_{Z_l}^f(\mathbf{x}_l) \right)
\end{aligned} \tag{F5a}$$

$$\begin{aligned}
895 \quad &= V_{Z_1, Z_2}^f(\mathbf{x}) - \frac{V_{Z_l}^f(\mathbf{x}_l)}{V_{Z_l}^f(\mathbf{x}_l) + V_{Z_l}^o(\mathbf{x}_l)} 2 \left(\sigma_{Z_2}^f(\mathbf{x}) \rho_{Z_2, Z_l, l}^f(\mathbf{x}) \sigma_{Z_1}^f(\mathbf{x}) \rho_{Z_1, Z_l, l}^f(\mathbf{x}) \right)
\end{aligned}$$

$$\begin{aligned}
&+ \frac{V_{Z_l}^f(\mathbf{x}_l)}{V_{Z_l}^f(\mathbf{x}_l) + V_{Z_l}^o(\mathbf{x}_l)} \sigma_{Z_1}^f(\mathbf{x}) \rho_{Z_1, Z_l, l}^f(\mathbf{x}) \sigma_{Z_2}^f(\mathbf{x}) \rho_{Z_2, Z_l, l}^f(\mathbf{x})
\end{aligned} \tag{F5b}$$

$$\begin{aligned}
&= V_{Z_1, Z_2}^f(\mathbf{x}) - \left(\sigma_{Z_2}^f(\mathbf{x}) \rho_{Z_2, Z_l, l}^f(\mathbf{x}) \sigma_{Z_1}^f(\mathbf{x}) \rho_{Z_1, Z_l, l}^f(\mathbf{x}) \right) \frac{V_{Z_l}^f(\mathbf{x}_l)}{V_{Z_l}^f(\mathbf{x}_l) + V_{Z_l}^o(\mathbf{x}_l)}.
\end{aligned} \tag{F5c}$$

The update of the variance in the multivariate situation leads to a new version of the PKFO1 as detailed in Algorithm 1.

900 *Author contributions.* AP and OP explored the multivariate extension of the PKF and designed the experiments. A part of the work has been co-supervised with VG during the master internship of AP.

Competing interests. The authors declare that they have no conflict of interest.

Acknowledgements. We would like to thank Annika Vogel, the other two anonymous referees and Zoltan Toth for their fruitful comments, which helped to improve the article. We thank Richard Ménard and Béatrice Josse for interesting discussions.

Algorithm 1 Sequential process building the analysis state and its error covariance matrix for the first-order PKF (PKFO1) with pseudo multivariate covariance model.

Require: Univariate fields of $\mathcal{X}_Z^f, \mathbf{s}_Z^f$ and V_Z^f for all species Z . Cross-covariance field $V_{Z_1 Z_2}^f$ of all pairs of species Z_1 and Z_2 . Variance $V_{Z_l, l}^o$ of the species Z_l and locations \mathbf{x}_l of the p observations to assimilate.

```

1: for each observation  $l$  do
2:   0 - Initialization of the intermediate quantities
3:    $\mathcal{Y}_{Z_l, l}^o = \mathcal{Y}_{Z_l}^o(\mathbf{x}_l), \mathcal{X}_{Z_l, l}^f = \mathcal{X}_{Z_l}^f(\mathbf{x}_l)$ 
4:    $V_{Z_l, l}^f = V_{Z_l, \mathbf{x}_l}^f, V_{Z_l, l}^o = V_{Z_l, \mathbf{x}_l}^o$ 
5:
6:   1 - Computation of the analysis univariate statistics
7:   for each species  $Z$  do
8:     a) Set the correlation function (auto or cross)
9:      $\rho_{ZZ_l, l}(\mathbf{x}) = \rho(V_{Z_l, Z}^f, V_{Z_l}^f, V_Z^f, \mathbf{s}_{Z_l}^f, \mathbf{s}_Z^f)(\mathbf{x}_l, \mathbf{x})$ 
10:
11:    b) Computation of the analysis state and its univariate error statistics
12:     $\mathcal{X}_{Z, \mathbf{x}}^a = \mathcal{X}_{Z, \mathbf{x}}^f + \sigma_{Z, \mathbf{x}}^f \rho_{ZZ_l, l}(\mathbf{x}) \frac{\sigma_{Z_l, l}^f}{V_{Z_l, l}^f + V_{Z_l, l}^o} (\mathcal{Y}_{Z_l, l}^o - \mathcal{X}_{Z_l, l}^f),$ 
13:     $V_{Z, \mathbf{x}}^a = V_{Z, \mathbf{x}}^f \left( 1 - [\rho_{ZZ_l, l}(\mathbf{x})]^2 \frac{V_{Z_l, l}^f}{V_{Z_l, l}^f + V_{Z_l, l}^o} \right)$ 
14:     $\mathbf{s}_{Z, \mathbf{x}}^a = \frac{V_{Z, \mathbf{x}}^a}{V_{Z, \mathbf{x}}^f} \mathbf{s}_{Z, \mathbf{x}}^f$ 
15:  end for
16:
17:  2 - Computation of the analysis multivariate statistics
18:  for each pair of species ( $Z_i, Z_j$ , with  $i < j$ ) do
19:    a) Set the cross-correlation functions
20:     $\rho_{Z_i Z_l, l}(\mathbf{x}) = \rho(V_{Z_l Z_i}^f, V_{Z_l}^f, V_{Z_i}^f, \mathbf{s}_{Z_l}^f, \mathbf{s}_{Z_i}^f)(\mathbf{x}_l, \mathbf{x})$ 
21:     $\rho_{Z_j Z_l, l}(\mathbf{x}) = \rho(V_{Z_l Z_j}^f, V_{Z_l}^f, V_{Z_j}^f, \mathbf{s}_{Z_l}^f, \mathbf{s}_{Z_j}^f)(\mathbf{x}_l, \mathbf{x})$ 
22:
23:    b) Compute the  $Z_i Z_j$  analysis cross-covariance field
24:     $V_{Z_i Z_j}^a(\mathbf{x}) = V_{Z_i Z_j}^f(\mathbf{x}) - \left( \sigma_{Z_j}^f(\mathbf{x}) \rho_{Z_j Z_l, l}(\mathbf{x}) \sigma_{Z_i}^f(\mathbf{x}) \rho_{Z_i Z_l, l}(\mathbf{x}) \right) \frac{V_{Z_l}^f(\mathbf{x}_l)}{V_{Z_l}^f(\mathbf{x}_l) + V_{Z_l}^o(\mathbf{x}_l)}$ 
25:  end for
26:
27:  3 - Update of the forecast state and its error statistics
28:  for each species  $Z$  do
29:     $\mathcal{X}_{Z, \mathbf{x}}^f \leftarrow \mathcal{X}_{Z, \mathbf{x}}^a$ 
30:     $V_{Z, \mathbf{x}}^f \leftarrow V_{Z, \mathbf{x}}^a$ 
31:     $\mathbf{s}_{Z, \mathbf{x}}^f \leftarrow \mathbf{s}_{Z, \mathbf{x}}^a$ 
32:  end for
33:
34:  for each pair of species ( $Z_i, Z_j$ ) do
35:     $V_{Z_i Z_j}^f(\mathbf{x}) \leftarrow V_{Z_i Z_j}^a(\mathbf{x})$ 
36:  end for
37: end for

```

Financial supporting The Toulouse Paul Sabatier University, and the doctoral school SDU2E (Sciences de l'Univers, de l'Environnement et
905 de l'Espace) supported Antoine Perrot's thesis. This work was supported by the French national programme LEFE/INSU grant "Multivariate
Parametric Kalman Filter" (MPKF).

References

- Aabaribaoune, M. E., Emili, E., and Guidard, V.: Estimation of the error covariance matrix for IASI radiances and its impact on the assimilation of ozone in a chemistry transport model, *Atmospheric Measurement Techniques*, 14, 2841–2856, <https://doi.org/10.5194/amt-14-2841-2021>, 2021.
- Amraoui, L. E., Sič, B., Piacentini, A., Marécal, V., Frebourg, N., and Attié, J.-L.: Aerosol data assimilation in the MOCAGE chemical transport model during the TRAQA/ChArMEx campaign: lidar observations, *Atmospheric Measurement Techniques*, 13, 4645–4667, <https://doi.org/10.5194/amt-13-4645-2020>, 2020.
- Anderson, J. L. and Anderson, S. L.: A Monte Carlo implementation of the nonlinear filtering problem to produce ensemble assimilations and forecasts, *Mon. Wea. Rev.*, 127, 2741–2758, 1999.
- Azzi, M., Johnson, G., and Cope, M.: An introduction to the generic reaction set photochemical smog mechanism, *Proceedings of the International Conference of the Clean Air Society of Australia and New Zealand*, 3, 451–462, 1992.
- Berre, L., Pannekoucke, O., Desroziers, G., Stefanescu, S., Chapnik, B., and Raynaud, L.: A variational assimilation ensemble and the spatial filtering of its error covariances: increase of sample size by local spatial averaging, in: *ECMWF Workshop on Flow-dependent aspects of data assimilation*, 11–13 June 2007., edited by ECMWF, pp. 151–168, Reading, UK, 2007.
- Cohn, S.: Dynamics of Short-Term Univariate Forecast Error Covariances, *Monthly Weather Review*, 121, 3123–3149, [https://doi.org/10.1175/1520-0493\(1993\)121<3123:DOSTUF>2.0.CO;2](https://doi.org/10.1175/1520-0493(1993)121<3123:DOSTUF>2.0.CO;2), 1993.
- Coman, A., Foret, G., Beekmann, M., Eremenko, M., Dufour, G., Gaubert, B., Ung, A., Schmechtig, C., Flaud, J. M., and Bergametti, G.: Assimilation of IASI partial tropospheric columns with an Ensemble Kalman Filter over Europe, *Atmospheric Chemistry Physics*, 12, 2513–2532, <https://doi.org/10.5194/acp-12-2513-2012>, 2012.
- Daley: *Atmospheric Data Analysis*, 1991.
- Derber, J. and Bouttier, F.: A reformulation of the background error covariance in the ECMWF global data assimilation system, *Tellus A*, 51, 195–221, <https://doi.org/10.3402/tellusa.v51i2.12316>, 1999.
- Eben, K., Jurus, P., Resler, J., Belda, M., Pelikán, E., Krüger, B. C., and Keder, J.: An ensemble Kalman filter for short-term forecasting of tropospheric ozone concentrations, *Quarterly Journal of the Royal Meteorological Society*, 131, 3313–3322, 2005.
- Emili, E., Gürol, S., and Cariolle, D.: Accounting for model error in air quality forecasts: an application of 4D-EnVar to the assimilation of atmospheric composition using QG-Chem 1.0, *Geoscientific Model Development*, 9, 3933–3959, <https://doi.org/10.5194/gmd-9-3933-2016>, 2016.
- Evensen, G.: Sequential data assimilation with a nonlinear quasi-geostrophic model using Monte Carlo methods to forecast error statistics, *Journal of Geophysical Research*, 99, 10 143–10 162, 1994.
- Evensen, G.: *Data Assimilation: The Ensemble Kalman Filter*, Springer-Verlag Berlin Heidelberg, <https://doi.org/10.1007/978-3-642-03711-5>, 2009.
- Fisher, M.: Background error covariance modelling, in: *Proc. ECMWF Seminar on "Recent developments in data assimilation for atmosphere and ocean"*, edited by ECMWF, pp. 45–63, Reading, UK, 2003.
- Gaubert, B., Coman, A., Foret, G., Meleux, F., Ung, A., Rouil, L., Ionescu, A., Candau, Y., and Beekmann, M.: Regional scale ozone data assimilation using an ensemble Kalman filter and the CHIMERE chemical transport model, *Geoscientific Model Development*, 7, 283–302, <https://doi.org/10.5194/gmd-7-283-2014>, 2014.

- Hauglustaine, D., Brasseur, G., Walters, S., Rasch, P., Müller, J.-F., Emmons, L., and Carroll, M.: MOZART: A global chemical transport model for ozone and related chemical tracers, *Journal of Geophysical Research*, 1032, 28 291–28 336, <https://doi.org/10.1029/98JD02398>, 1998.
- 945
- Haussaire, J.-M. and Bocquet, M.: A low-order coupled chemistry meteorology model for testing online and offline data assimilation schemes: L95-GRS (v1.0), *Geoscientific Model Development*, 9, 393–412, <https://doi.org/10.5194/gmd-9-393-2016>, 2016.
- Houtekamer, P. and Mitchell, H.: A sequential ensemble Kalman filter for atmospheric data assimilation, *Monthly Weather Review*, 129, 123–137, [https://doi.org/10.1175/1520-0493\(2001\)129<0123:ASEKFF>2.0.CO;2](https://doi.org/10.1175/1520-0493(2001)129<0123:ASEKFF>2.0.CO;2), 2001.
- 950 Houtekamer, P. L. and Mitchell, H. L.: Data Assimilation Using an Ensemble Kalman Filter Technique, *Monthly Weather Review*, 126, 796–811, [https://doi.org/10.1175/1520-0493\(1998\)126<0796:dauack>2.0.co;2](https://doi.org/10.1175/1520-0493(1998)126<0796:dauack>2.0.co;2), 1998.
- Josse, B., Simon, P., and Peuch, V.-H.: Radon global simulations with the multiscale chemistry and transport model MOCAGE, *Tellus*, 56, 339–356, 2004.
- Kalman, R. E.: A New Approach to Linear Filtering and Prediction Problems, *Journal Basic Engineering*, 82, 35–45, <https://doi.org/10.1115/1.3662552>, 1960.
- 955
- Lesieur, M.: *Turbulence in Fluids*, Springer.
- Lorenz, E. N.: Deterministic nonperiodic flow, *Journal Atmospheric Sciences*, 20, 130–141, [https://doi.org/10.1175/1520-0469\(1963\)020<0130:DNF>2.0.CO;2](https://doi.org/10.1175/1520-0469(1963)020<0130:DNF>2.0.CO;2), 1963.
- Marécal, V., Peuch, V.-H., Andersson, C., Andersson, S., Arteta, J., Beekmann, M., Benedictow, A., Bergström, R., Bessagnet, B., Cansado, A., Chéroux, F., Colette, A., Coman, A., Curier, R. L., van der Gon, H. A. C. D., Drouin, A., Elbern, H., Emili, E., Engelen, R. J., Eskes, H. J., Foret, G., Friese, E., Gauss, M., Giannaros, C., Guth, J., Joly, M., Jaumouillé, E., Josse, B., Kadyrov, N., Kaiser, J. W., Krajsek, K., Kuenen, J., Kumar, U., Liora, N., Lopez, E., Malherbe, L., Martinez, I., Melas, D., Meleux, F., Menut, L., Moinat, P., Morales, T., Parmentier, J., Piacentini, A., Plu, M., Poupkou, A., Queguiner, S., Robertson, L., Rouil, L., Schaap, M., Segers, A., Sofiev, M., Tarasson, L., Thomas, M., Timmermans, R., Valdebenito, Á., van Velthoven, P., van Versendaal, R., Vira, J., and Ung, A.: A regional air quality forecasting system over Europe: the MACC-II daily ensemble production, *Geoscientific Model Development*, 8, 2777–2813, <https://doi.org/10.5194/gmd-8-2777-2015>, 2015.
- 960
- 965
- Ménard, R., Deshaies-Jacques, M., and Gasset, N.: A comparison of correlation-length estimation methods for the objective analysis of surface pollutants at Environment and Climate Change Canada, *Journal Air Waste Management Association*, <https://doi.org/10.1080/10962247.2016.1177620>, 2016.
- 970 Ménard, R., Skachko, S., and Pannekoucke, O.: Numerical discretization causing error variance loss and the need for inflation, *Quarterly Journal of the Royal Meteorological Society*, <https://doi.org/10.1002/qj.4139>, 2021.
- Meurer, A., Smith, C. P., Paprocki, M., Čertík, O., Kirpichev, S. B., Rocklin, M., Kumar, A., Ivanov, S., Moore, J. K., Singh, S., Rathnayake, T., Vig, S., Granger, B. E., Muller, R. P., Bonazzi, F., Gupta, H., Vats, S., Johansson, F., Pedregosa, F., Curry, M. J., Terrel, A. R., Roučka, Š., Saboo, A., Fernando, I., Kulal, S., Cimrman, R., and Scopatz, A.: SymPy: symbolic computing in Python, *PeerJ Computer Science*, 3, e103, <https://doi.org/10.7717/peerj-cs.103>, 2017.
- 975
- Mirouze, I. and Weaver, A. T.: Representation of correlation functions in variational assimilation using an implicit diffusion operator, *Quarterly Journal of the Royal Meteorological Society*, 136, 1421–1443, <https://doi.org/10.1002/qj.643>, 2010.
- Miyazaki, K., Eskes, H. J., Sudo, K., Takigawa, M., van Weele, M., and Boersma, K. F.: Simultaneous assimilation of satellite NO₂, O₃, CO, and HNO₃ data for the analysis of tropospheric chemical composition and emissions, *Atmospheric Chemistry and Physics*, 12, 9545–9579, <https://doi.org/10.5194/acp-12-9545-2012>, 2012.
- 980

- Paciorek, C. and Schervish, M.: Spatial Modelling Using a New Class of Nonstationary Covariance Functions, *Environmetrics*, 17, 483–506, <https://doi.org/10.1002/env.785>, 2006.
- Pannekoucke, O.: An anisotropic formulation of the parametric Kalman filter assimilation, *Tellus A: Dynamic Meteorology and Oceanography*, 73, 1–27, <https://doi.org/10.1080/16000870.2021.1926660>, 2021.
- 985 Pannekoucke, O. and Arbogast, P.: SymPKF (v1.0): a symbolic and computational toolbox for the design of parametric Kalman filter dynamics, *Geoscientific Model Development*, 14, 5957–5976, <https://doi.org/10.5194/gmd-14-5957-2021>, 2021.
- Pannekoucke, O. and Fablet, R.: PDE-NetGen 1.0: from symbolic partial differential equation (PDE) representations of physical processes to trainable neural network representations, *Geoscientific Model Development*, 13, 3373–3382, <https://doi.org/10.5194/gmd-13-3373-2020>, 2020.
- 990 Pannekoucke, O. and Massart, S.: Estimation of the local diffusion tensor and normalization for heterogeneous correlation modelling using a diffusion equation., *Quarterly Journal of the Royal Meteorological Society.*, 134, 1425–1438, <https://doi.org/10.1002/qj.288>, 2008.
- Pannekoucke, O., Ricci, S., Barthelemy, S., Ménard, R., and Thual, O.: Parametric Kalman filter for chemical transport models, *Tellus A: Dynamic Meteorology and Oceanography*, 68, 31 547, <https://doi.org/10.3402/tellusa.v68.31547>, 2016.
- Pannekoucke, O., Bocquet, M., and Ménard, R.: Parametric covariance dynamics for the nonlinear diffusive Burgers’ equation, *Nonlinear*
- 995 *Processes in Geophysics*, 2018, 1–21, <https://doi.org/https://doi.org/10.5194/npg-2018-10>, 2018.
- Pannekoucke, O., Ménard, R., El Aabaribaoune, M., and Plu, M.: A methodology to obtain model-error covariances due to the discretization scheme from the parametric Kalman filter perspective, *Nonlinear Processes in Geophysics*, 28, 1–22, <https://doi.org/10.5194/npg-28-1-2021>, 2021.
- Peiro, H., Emili, E., Cariolle, D., Barret, B., and Flochmoën, E. L.: Multi-year assimilation of IASI and MLS ozone retrievals: variability of tropospheric ozone over the tropics in response to ENSO, *Atmospheric Chemistry and Physics*, 18, 6939–6958, <https://doi.org/10.5194/acp-18-6939-2018>, 2018.
- 1000 Purser, R., Wu, W.-S., D.Parrish, and Roberts, N.: Numerical aspects of the application of recursive filters to variational statistical analysis. Part II: Spatially inhomogeneous and anisotropic general covariances, *Monthly Weather Review*, 131, 1536–1548, <https://doi.org/10.1175//2543.1>, 2003.
- 1005 Sabathier, M., Pannekoucke, O., and Maget, V.: Boundary Conditions for the Parametric Kalman Filter forecast, to submit, 2022.
- Tang, X., Zhu, J., Wang, Z. F., and Gbaguidi, A.: Improvement of ozone forecast over Beijing based on ensemble Kalman filter with simultaneous adjustment of initial conditions and emissions, *Atmospheric Chemistry and Physics*, 11, 12 901–12 916, <https://doi.org/10.5194/acp-11-12901-2011>, 2011.
- Voshtani, S., Ménard, R., Walker, T. W., and Hakami, A.: Assimilation of GOSAT Methane in the Hemispheric CMAQ; Part I: Design of the
- 1010 *Assimilation System*, *Remote Sensing*, 14, 371, <https://doi.org/10.3390/rs14020371>, 2022a.
- Voshtani, S., Ménard, R., Walker, T. W., and Hakami, A.: Assimilation of GOSAT Methane in the Hemispheric CMAQ; Part II: Results Using Optimal Error Statistics, *Remote Sensing*, 14, 375, <https://doi.org/10.3390/rs14020375>, 2022b.
- Weaver, A. and Courtier, P.: Correlation modelling on the sphere using a generalized diffusion equation (Tech. Memo. ECMWF, num. 306), *Quarterly Journal of the Royal Meteorological Society*, 127, 1815–1846, <https://doi.org/10.1002/qj.49712757518>, 2001.
- 1015 Weaver, A., Deltel, C., Machu, E., Ricci, S., and Daget, N.: A multivariate balance operator for variational ocean data assimilation, *Quarterly Journal of the Royal Meteorological Society*, 131, 3605 – 3625, <https://doi.org/10.1256/qj.05.119>, 2006.
- Weisstein, E. W.: Courant-Friedrichs-Lewy Condition, 2002.

Whitaker, J. and Hamill, M.: Ensemble Data Assimilation without Perturbed Observations, *Monthly Weather Review*, 130, [https://doi.org/10.1175/1520-0493\(2002\)130<1913:EDAWPO>2.0.CO;2](https://doi.org/10.1175/1520-0493(2002)130<1913:EDAWPO>2.0.CO;2), 2003.

1020 Whitham, G. B.: *Linear and nonlinear waves*, Wiley, 1999.

Multivariate forecast statistics for GRS: Ens. estimation ($N_e=1600$, black dashed lines) and PKF (colored lines)

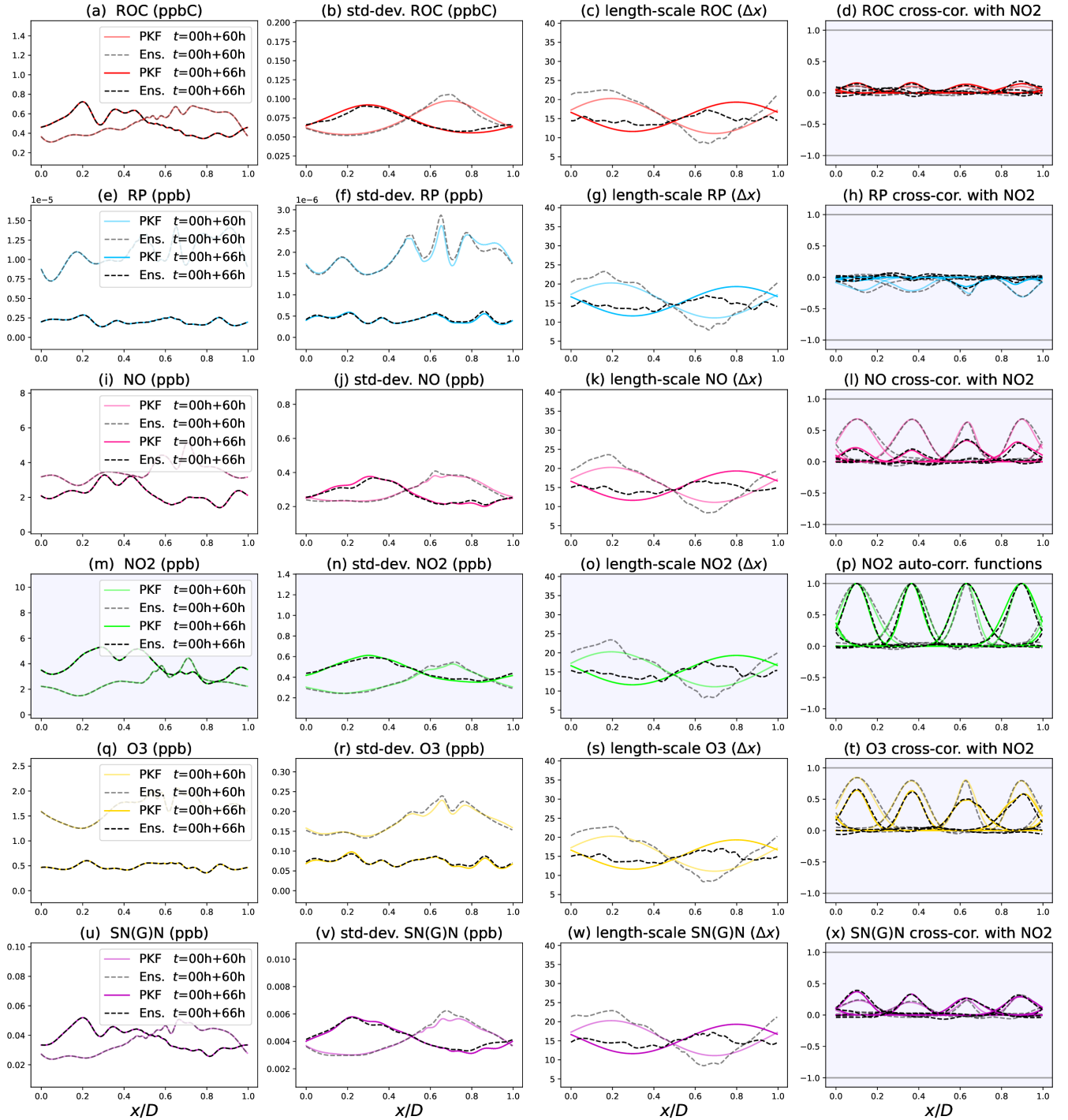


Figure 9. Multivariate forecasts statistics for the GRS-CTM, PKF outputs (colored lines) and ensemble estimations from $N_e = 1600$ forecasts (black dashed lines) for times $t = 00h + \{60, 66\}h$. As we consider a simulation that starts at midnight of day 0, $t = 00h + 60h$ (slight transparency on the curves) corresponds to midday of day 2, and $t = 00h + 66h$ (no transparency) to 18h00 of day 2. From left to right, the columns correspond to the forecasts of: the mean concentration, the standard-deviation, the length-scales (normalized by Δx), and the correlation functions (*auto* and *cross*) with NO₂ at locations $x = [0.1, 0.36, 0.63, 0.9]D$, for each of the six species (rows).

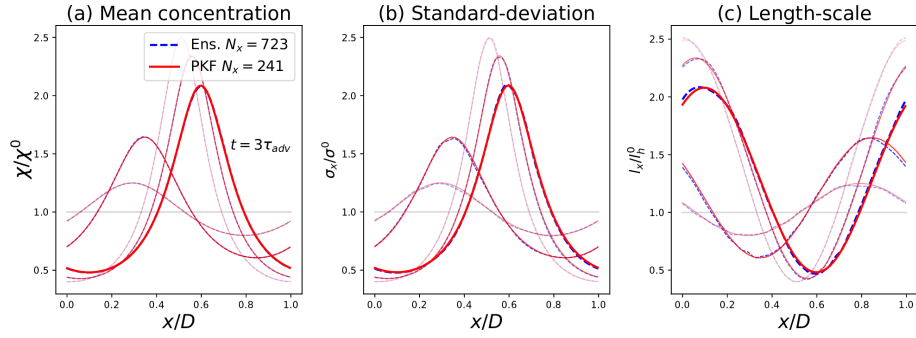


Figure A1. Same experiment as Fig. 2, except the EnKF forecast has been simulated using a higher grid definition ($N_x = 723$) to reduce numerical model error.

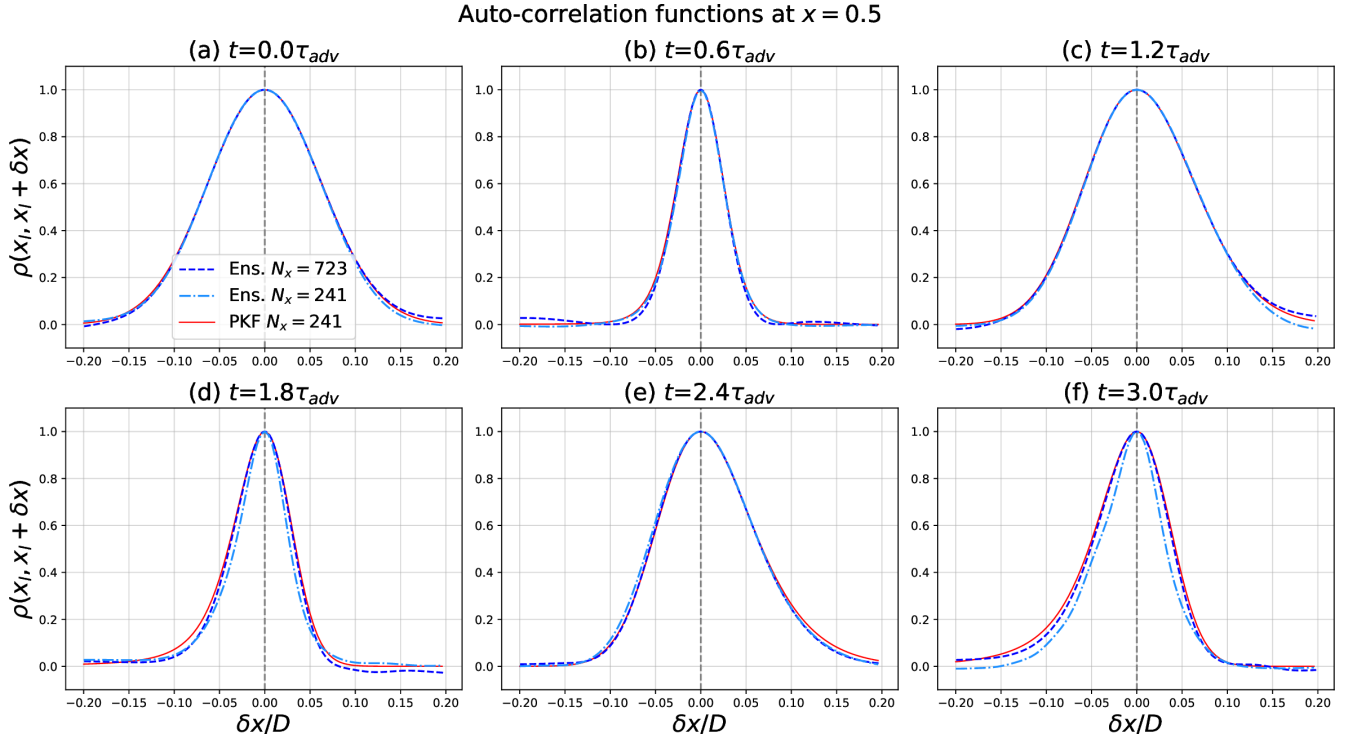


Figure B1. Correlation functions at location $x_l = 0.5$ and times $t = [0.0, 0.6, 1.2, 1.8, 2.4, 3.0]\tau_{adv}$, computed with PKF correlation model fitted with low resolution ($N_x = 241$) PKF forecast for error statistics (red lines) and diagnosed on the low-resolution ($N_x = 241$) ensemble (cyan dash-dotted lines) and high resolution ($N_x = 723$) ensemble (blue dashed lines), of ensemble size $N_e = 6400$.

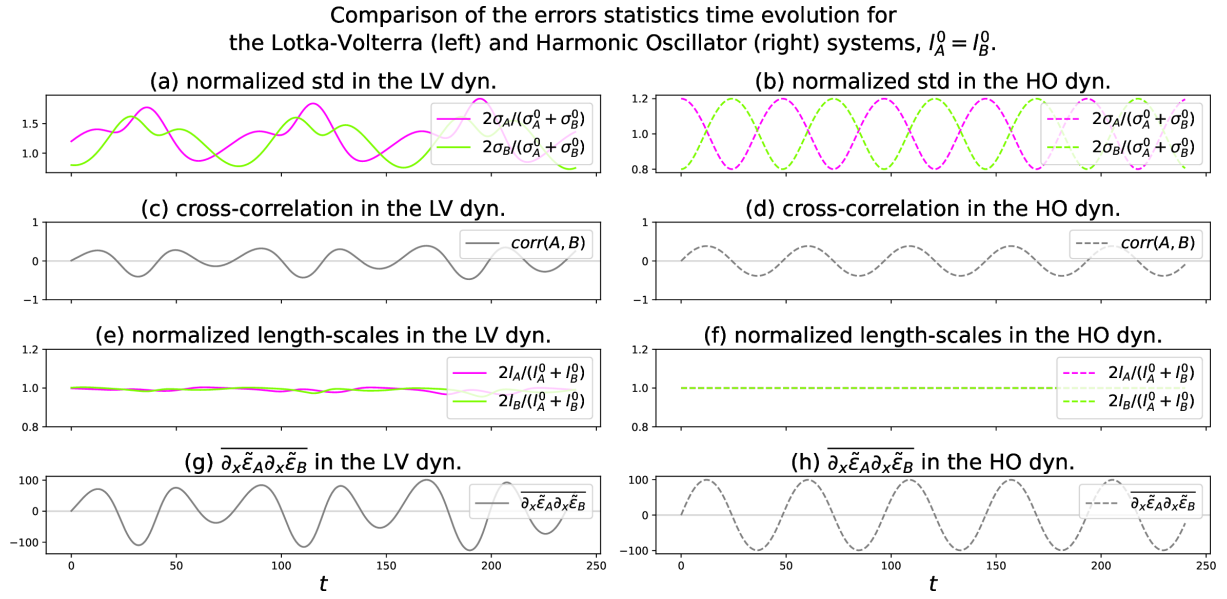


Figure D1. Time series of the spatial average of the error statistics: from the ensemble forecast with $N_e = 1600$ for Lotka-Volterra (LV, left panels) and Harmonic Oscillator analytical solutions (HO, right panels). Equal initial length-scales: $l_A^0 = l_B^0 = 45\Delta x$.

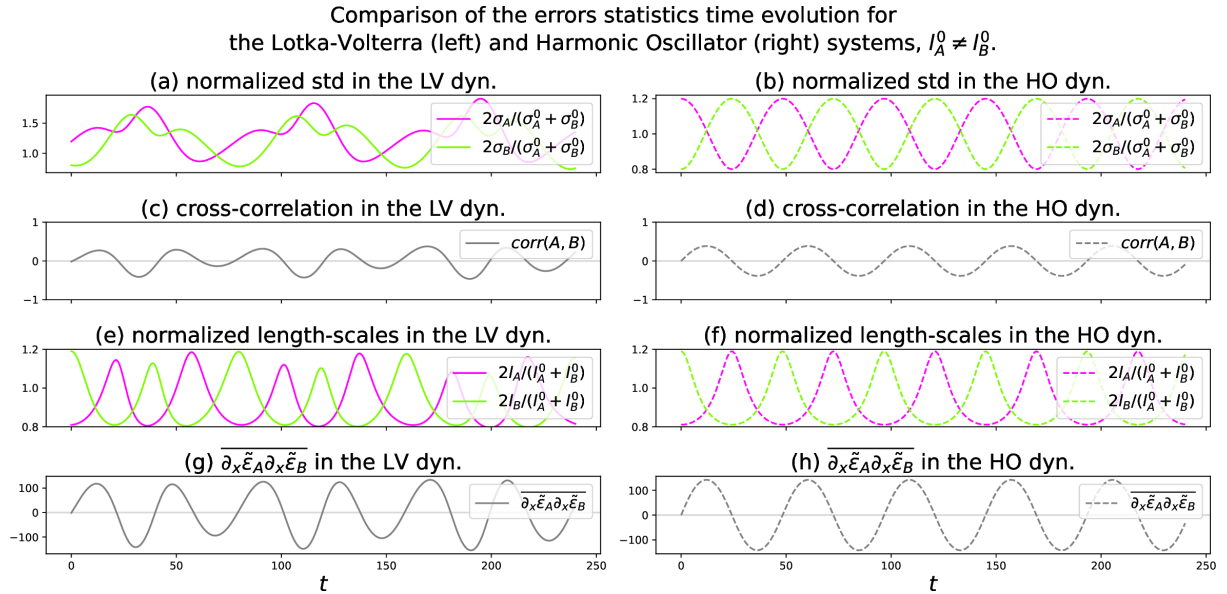


Figure D2. Time series of the spatial average of the error statistics: from the ensemble forecast with $N_e = 1600$ for Lotka-Volterra (LV, left panels) and Harmonic Oscillator analytical solutions (HO, right panels). Different initial length-scales: $l_A^0 = 45\Delta x$ and $l_B^0 = 66\Delta x$.

Relative contributions by term and process in the anisotropy dynamics, $l_A^0 = l_B^0$

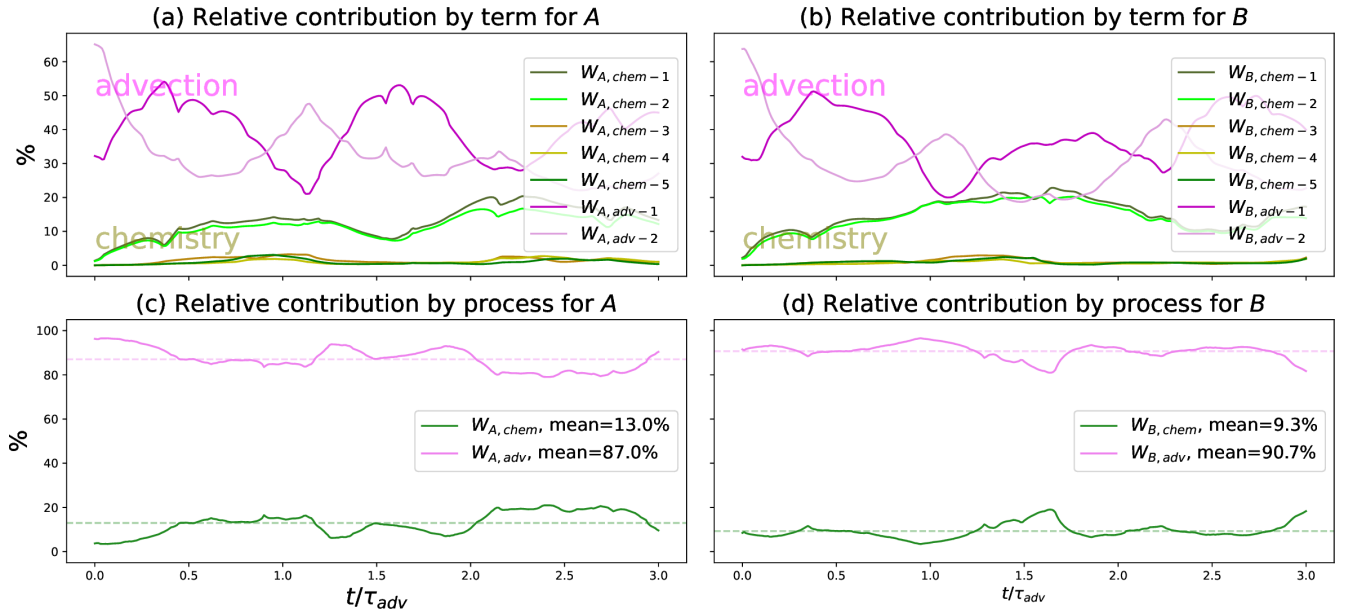


Figure D3. Numerical results for the case $l_A^0 = l_B^0 = 45\Delta x$. Time evolution for the relative contribution by term (resp. by process) computed from Eq. (D6) (from Eq. (D7)) involved in the anisotropy dynamics for species *A* and *B* on panels (a) and (b) (resp. panels (c) and (d)).

Relative contributions by term and process in the anisotropy dynamics, $l_A^0 \neq l_B^0$

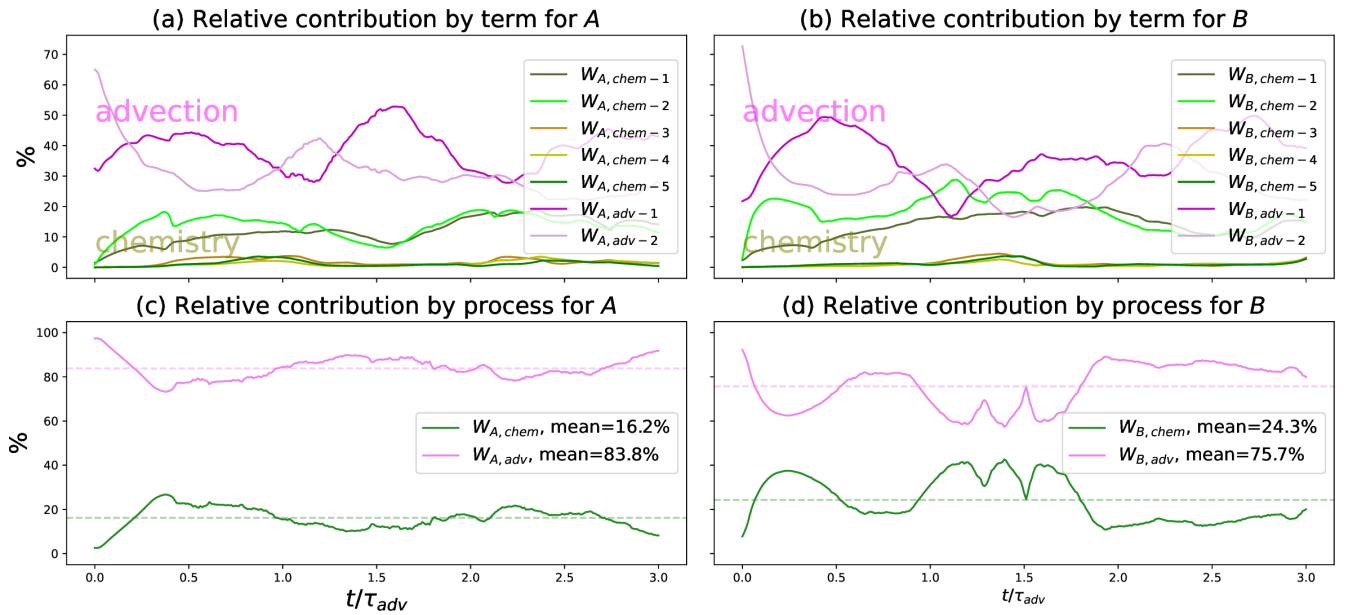


Figure D4. Numerical results for the case $l_A^0 = 45\Delta x$ and $l_B^0 = 66\Delta x$. Time evolution for the relative contribution by term (resp. by process) computed from Eq. (D6) (from Eq. (D7)) involved in the anisotropy dynamics for species *A* and *B* on panels (a) and (b) (resp. panels (c) and (d)).